Engineering Structures 292 (2023) 116501

Contents lists available at ScienceDirect

Engineering Structures

journal homepage: www.elsevier.com/locate/engstruct

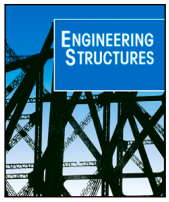

A fiber beam element based on plastic and damage models for prestressed concrete structures

Luca Parente [a,*], Daniela Addessi [b], Enrico Spacone [a]

[a] Department of Engineering and Geology, G. D'Annunzio University of Chieti-Pescara, Viale Pindaro 42, 65127, Italy
[b] Department of Structural and Geotechnical Engineering, Sapienza University of Rome, Via Eudossiana 18, 00184, Italy

ARTICLE INFO

Keywords:
Beam finite element
Fiber section
Damage
Plasticity
Regularization
Prestressed concrete
Cyclic analysis
Nonlinear analysis

ABSTRACT

Modeling of prestressed concrete beams and their degrading processes are relevant issues in the assessment of existing structures and infrastructures, particularly for bridges. This work focuses on the formulation and validation of a fiber beam finite element for prestressed concrete structural elements that accounts for nonlinear material behavior and time-dependent phenomena. The element is a 3D Timoshenko beam that follows a force-based approach. A fiber discretization of the cross-section is used to model concrete, steel reinforcements and prestressing cables based on damage and plasticity for concrete, and plasticity for steel through three-dimensional constitutive laws. The steel fibers are fully bonded. Strain-softening in the concrete requires an appropriate regularization procedure. The tendons are treated as additional fibers with prestressing applied as initial strain of the relevant fibers. No additional discretization is required except for the description of the tendons' profile. Time-dependent phenomena such as creep, shrinkage and cable relaxation are taken into account. The proposed model is implemented in the OpenSees computational framework to carry out specific validation tests and demonstrate the element potential.

1. Introduction

Beam elements can be suitably used in a large number of structural cases and represent the best compromise between accuracy and computational cost based on limited amount of degrees of freedom. This work presents a new prestressed concrete (PC) beam finite element (FE), based on existing force-based (FB) formulations for reinforced concrete elements that takes into account the interaction between normal, bending and shear stresses, and adds the main effects of prestressing, including time-dependent phenomena in steel and concrete. The proposed element is applied here to beams, but given the versatile formulation, its use can extend to a large number of possible cases, including precast structures.

In the last decades, the FB approach for beam elements (Zeris and Mahin [1], Spacone et al. [2] and Addessi and Ciampi [3]) has shown major advantages over the displacement-based (DB) formulation (Åldstedt and Bergand [4]) since the profile of the element displacements under large forces is often localized and difficult to describe with polynomial interpolations used in DB formulations. The FB formulations describe the section generalized stresses in a statically determinate basic system without rigid body modes, thus equilibrium is enforced in strong form and the internal force distributions along the element are exact. More advanced formulations, such as those proposed in Spacone and Limkatanyu [5] and generalized in Taylor et al. [6], allow for the distinct interpolation of forces and displacements with more sophisticated functions: these formulations are particularly interesting for elements with bond–slip. Feng et al. propose similar FB fiber beam element formulations both in the 2D field [7,8] and in the 3D framework [9]. This latter considers curvature-shear based displacement interpolation and geometrical nonlinear effects for accurate strain description. In addition to their previous works, where nonlocal regularization procedures are proposed to overcome localization issues, such as the implicit-gradient formulation, in [9] local procedures are presented as an alternative underlying their ease of application.

In FE programs, it is common to model prestressed structures either by using loads acting on the reinforced concrete member or large number of elements to discretize the reinforced concrete beam and the individual tendon trusses (e.g., Aalami [10], Picard et al. [11]). Beams with external tendons were thoroughly studied by Ayoub, Filippou and co-workers [12–15]. The prestressing is modeled by introducing an enriched element formulation. A mixed approach is used to evaluate the section displacements and introduce a bond relationship between the prestressing trusses and the reinforced concrete beam, the latter including a classic fiber section model. The above formulations require a dense discretization of the elements to generate internal nodes where

* Corresponding author.
E-mail address: luca.parente@uniroma1.it (L. Parente).

https://doi.org/10.1016/j.engstruct.2023.116501
Received 16 January 2023; Received in revised form 27 April 2023; Accepted 15 June 2023
Available online 10 July 2023

bond is transferred. Other FE analyses of PC structures are found, for example Vu et al. [16], who present a model for the structural response of post-tensioned beams based on the definition of a FE with homogenous average inertia. In Kim and Lee [17] a flexural model for continuous unbonded post-tensioned members is proposed. Moreira et al. [18] model the tendon as a single polygonal element, embedded in a specified subset of frame elements. Some of these works include the bond–slip, but some issues remain. The element is usually formulated with a DB approach, thus a dense mesh must be used, and the Euler–Bernoulli formulation is used, therefore the shear strains are neglected. In this work, the stresses induced by the prestressing are added at the fiber level through equivalent initial strains, as proposed by Doty [19]. The computational burden added is negligible since it only requires the insertion of new fibers and few other features.

Time-dependent effects must be considered, since they increase structural deformability and thus deflection over time, considerably affecting the serviceability limit states. There are FE studies that include concrete creep and shrinkage, and tendon relaxation phenomena, such as in Kwak and Seo [20], where the creep and shrinkage effects in concrete are considered according to a recursive algorithm based on the expansion of the compliance function. In Au and Si [21], a relaxation model for steel tendons is proposed based on the equivalent creep coefficient to estimate the losses in the cable forces. In the studies by Lou et al. [22,23], the effects of long-term phenomena on the nonlinear analysis of PC girders within a DB formulation are included.

In this work, a single element can be used to represent most cases. Starting from the older fiber section models proposed by the second and third authors, the 3D FB formulation is extended to account for the shear components and include the tendon effects. The prestressing cables are treated as additional, fully bonded fibers in each section. This way, complex geometry tendon layouts can also be modeled with a small number of elements. The proposed formulation is particularly suitable for the analysis of bridge beams with internal cables, precast girders and pillars for civil and building works and other constructions where the system involves the use of fully bonded cables. Compatibility of displacements and strains must hold between cables and concrete in any section along the longitudinal direction. In case of external prestressing, modeling alternatives can be followed, such as the use of eccentric beam and truss elements connected at the nodes located at the anchor points.

The concrete constitutive law is based on the 3D isotropic plastic damage model developed for cementicious brittle materials proposed by Addessi et al. [24] and then enriched for masonry by Gatta et al. [25] and for concrete by Di Re et al. [26]. It adopts a macromechanical approach by introducing two different damage variable which describe the damaging process for prevailing tensile or compressive strain states. The growth of plastic strains is ruled by a Drucker–Prager [27] yield limit function. Concerning computational aspects, to link a 3D material to every fiber of a Timoshenko beam, where only three strain components are necessary, a condensation algorithm is implemented [28]. This step relies on the assumption of the beam theory where the three stresses outside the longitudinal axis are assumed as zero. A regularization technique is introduced to eliminate the pathological mesh-dependency issues. Rather than applying the nonlocal integral formulation, as proposed in [25], a simple local procedure is adopted which acts on the integration scheme, similar to those proposed by Scott et al. [29,30], Addessi and Ciampi in [3].

The 3D beam FE proposed in this work is implemented in the open-source computational platform OpenSees [31] through the aid of STKO [32]. New classes are created for the new 3D damage-plastic constitutive law for concrete, the condensation algorithm, the regularization technique and a new load command which applies prestressing and time-dependent properties to the elements. The 3D fiber section and the FB beam formulation are modified to accommodate the new properties.

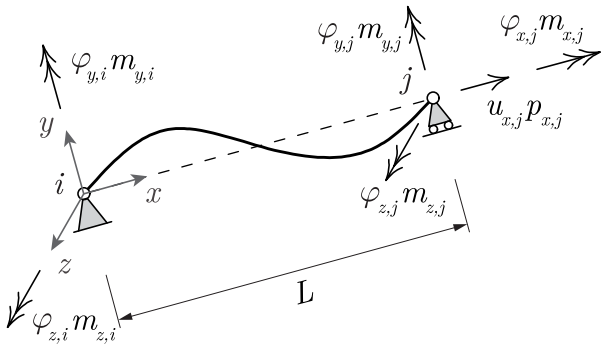

Fig. 1. 3D FB beam element without rigid body modes in local basic reference system: nodal displacements and forces.

Following this introduction, the FB element formulation is detailed in Section 2. In Section 3, the beam model with the prestressing cables is presented, introducing the steps followed to input the tendons in the fiber sections and compute the time-dependent effects. Section 4 briefly recalls the 3D damage-plastic constitutive law used for concrete, which is based on [26] and uses a full 3D strain description [28]. Computational aspects are detailed in Section 5. To validate the proposed PC element, various experimental and analytical results are compared and discussed in Section 6. Prestressed beams from Hussien et al. [33] and Breckenridge and Bugg [34] are tested with static analyses in one case and pseudo-static analyses in the other, including time-dependent effects.

2. 3D beam finite element formulation

The proposed beam FE is based on the 3D FB approach and assumes small displacements and strains and full bond between steel and concrete fibers. The element is shown in Fig. 1 in its local basic reference system where the rigid body modes are removed by considering a simply supported configuration. It is a 2-node FE with 6 displacement degrees of freedom at each end node. The local x axis is directed from node i to node j, while the y and z directions coincide with the cross-section principal axes of inertia.

The element nodal force vector $\mathbf{q}$ is defined as:

$$\mathbf{q} = [p_{x,j} \quad m_{y,i} \quad m_{y,j} \quad m_{z,i} \quad m_{z,j} \quad m_{x,j}]^T \tag{1}$$

where $p_{x,j}$ is the axial force, $m_{y,i}$, $m_{y,j}$, $m_{z,i}$, $m_{z,j}$ and $m_{x,i}$ are the moments at nodes i and j around the x, y, z local axes. The element basic displacement vector $\mathbf{v}$, work-conjugate to the nodal force vector $\mathbf{q}$, is:

$$\mathbf{v} = [u_{x,j} \quad \varphi_{y,i} \quad \varphi_{y,j} \quad \varphi_{z,i} \quad \varphi_{z,j} \quad \varphi_{x,j}]^T \tag{2}$$

where $u_{x,j}$ is the axial displacement of node j, while $\varphi_{y,i}$, $\varphi_{y,j}$, $\varphi_{z,i}$, $\varphi_{z,j}$ and $\varphi_{x,j}$ are the rotations at nodes i and j around the x, y, z local axes.

Following the classical FB formulation, the equilibrium equation is given by:

$$\mathbf{s}(x) = \mathbf{b}(x)\mathbf{q} + \mathbf{s}_q(x) \tag{3}$$

where vector $\mathbf{s}(x)$ contains the generalized section stresses:

$$\mathbf{s}(x) = [N(x) \quad M_y(x) \quad M_z(x) \quad V_z(x) \quad V_y(x) \quad T(x)]^T \tag{4}$$

where $N(x)$ is the axial force, $M_y(x)$ and $M_z(x)$ the bending moments around the y and z axes, respectively, $V_z(x)$ and $V_y(x)$ are the shear forces in the y and z directions, $T(x)$ is the torque around the x axis. $\mathbf{b}(x)$ is the equilibrium matrix that links the section generalized stresses

$\mathbf{s}(x)$ to the element nodal forces $\mathbf{q}$ and is defined as follows:

$$\mathbf{b}(x) = \begin{bmatrix} 1 & 0 & 0 & 0 & 0 & 0 \\ 0 & -1+\frac{x}{L} & \frac{x}{L} & 0 & 0 & 0 \\ 0 & 0 & 0 & -1+\frac{x}{L} & \frac{x}{L} & 0 \\ 0 & \frac{1}{L} & \frac{1}{L} & 0 & 0 & 0 \\ 0 & 0 & 0 & \frac{1}{L} & \frac{1}{L} & 0 \\ 0 & 0 & 0 & 0 & 0 & 1 \end{bmatrix} \tag{5}$$

and $\mathbf{s}_q(x)$ is the vector of the generalized section stresses in equilibrium with the distributed loads.

The work-conjugate generalized section strain vector $\mathbf{e}(x)$ is:

$$\mathbf{e}(x) = [\varepsilon_G(x) \quad \chi_y(x) \quad \chi_z(x) \quad \gamma_z(x) \quad \gamma_y(x) \quad \theta(x)]^T \tag{6}$$

where $\varepsilon_G(x)$ is the axial strain, $\chi_y(x)$ and $\chi_z(x)$ are the curvatures around the y and z axes, respectively, $\gamma_y(x)$ and $\gamma_z(x)$ are the shear strains in the y and z directions, respectively, and $\theta(x)$ is the torsion strain around the x axis.

The section constitutive relationship, according to the FB formulation, is:

$$\dot{\mathbf{e}}(x) = \mathbf{f}(x)\dot{\mathbf{s}}(x) \tag{7}$$

where "˙" indicates first derivative, $\mathbf{f}(x)$ is the section tangent flexibility matrix, computed as the inverse of the section tangent stiffness $\mathbf{k}(x)$. This latter is obtained from the section state determination, that relies on the fiber section model briefly recalled in the next session.

The virtual work principle leads to the following element equation:

$$\dot{\mathbf{v}} = \mathbf{F}\dot{\mathbf{q}} \tag{8}$$

where $\mathbf{F}$ is the element tangent flexibility matrix:

$$\mathbf{F} = \int_0^L \mathbf{b}^T(x)\mathbf{f}(x)\mathbf{b}(x)dx \tag{9}$$

3. Fiber section model with prestressing effects

In the proposed biaxial fiber section, the fiber strains are computed from the section generalized strains $\mathbf{e}(x)$. The prestressing effects are included by introducing the tendons as individual fibers. Depending on the tendon profile, in a given section the tendon fibers are not necessarily parallel to the x local axis, but can have a slope with respect to the cross-section, as formerly proposed in [19]. An initial input strain is assigned to the tendon fiber. The following compatibility equation applies:

$$\boldsymbol{\varepsilon}(x, y, z) = \mathbf{a}_s(y, z)\ \mathbf{e}(x) + \boldsymbol{\varepsilon}_0(x, y, z) \tag{10}$$

or:

$$\begin{Bmatrix} \varepsilon_x \\ \gamma_{xy} \\ \gamma_{xz} \end{Bmatrix} = \begin{bmatrix} 1 & -y & z & 0 & 0 & 0 \\ 0 & 0 & 0 & 0 & s_y(y) & -z \\ 0 & 0 & 0 & s_z(z) & 0 & y \end{bmatrix} \begin{Bmatrix} \varepsilon_G \\ \chi_y \\ \chi_z \\ \gamma_z \\ \gamma_y \\ \theta \end{Bmatrix} + \begin{Bmatrix} \varepsilon_0 \\ 0 \\ 0 \end{Bmatrix} \tag{11}$$

Note that the vector $\boldsymbol{\varepsilon}_0$ contains only the axial elongation ε_0, that is the initial axial elastic strain applied to the strands through the prestressing jacks, assuming a linear elastic behavior. ε_0 can be evaluated from the jacks' imposed stress σ_0, or axial force N_0, the tendon geometry and Young's modulus. The approach works both for pre-tensioned and post-tensioned beams assuming, in the latter case, full bond after grouting. The Timoshenko formulation only includes two average shear strains per direction (γ_y and γ_z). In this work parabolic shear strain distributions for rectangular sections are used instead. The terms $s_y(y)$ and $s_z(z)$ in Eq. (11) are shape functions that depend on the fiber location (y, z) and define the following parabolic shear strain distributions:

$$s_y(y) = \frac{\gamma_{xy}(y)}{\gamma_y} = \frac{3}{2}\left[1 - \left(\frac{2y}{H_y}\right)^2\right] \tag{12}$$

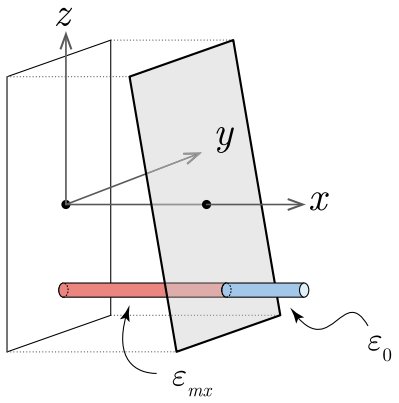

Fig. 2. Tendon fiber overall strain ε, computed as the sum of the fiber compatible strain ε_{mx} and the initial fiber strain ε_0.

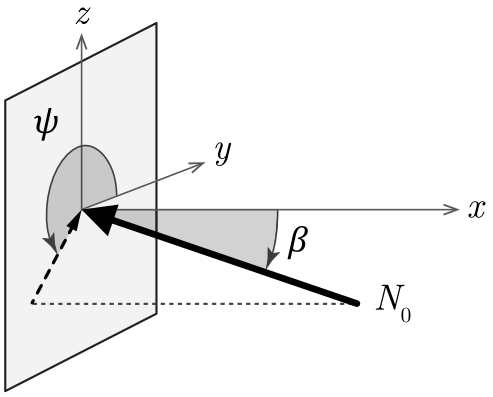

Fig. 3. Angles between the tendon and the section axes. β is the angle about the x axis, ψ is about the y axis.

$$s_z(z) = \frac{\gamma_{xz}(z)}{\gamma_z} = \frac{3}{2}\left[1 - \left(\frac{2z}{H_z}\right)^2\right] \tag{13}$$

where H_y and H_z are the section width and depth in the y and z directions, respectively, while γ_y and γ_z are the average shear strains in the xy and xz planes, respectively. The terms $s_y(y)$ and $s_z(z)$ can be calculated to obtain shear strains in any section. An example of a different shear distribution is used for the double-T beams in Sections 6.2 and 6.4.

The resulting strains in Eq. (10) can also be expressed as the sum of two contributions, one coming from the compatible section strains $\boldsymbol{\varepsilon}_m$ and one due to the initial prestressing $\boldsymbol{\varepsilon}_0$, as shown in Fig. 2:

$$\boldsymbol{\varepsilon} = \boldsymbol{\varepsilon}_m + \boldsymbol{\varepsilon}_0 \tag{14}$$

The initial fiber strain ε_0 is positive (tension). However, the cables in the beam are usually placed with an inclination that varies along the beam depending on the tendon geometry. Thus, the strain field of the tendon fibers is projected on the section reference system x, y, z to account for the slopes of the tendon at the given section. It is assumed that the axial force of the tendon has the inclination β with respect to the x axis and ψ with respect to the y axis on the yz plane, as shown in Fig. 3. For each tendon fiber, the generalized section stress components can be obtained by defining a rotation matrix $\mathbf{R}$ as the product of two rotation matrices $\mathbf{R}_\beta$ and $\mathbf{R}_\psi$ about β and ψ, respectively:

$$\mathbf{R} = \mathbf{R}_\beta \mathbf{R}_\psi \tag{15}$$

$$\mathbf{R} = \begin{bmatrix} \cos\beta & 0 & -\sin\beta \\ -\sin\beta & \cos\psi & -\cos\beta\sin\psi \\ \cos\psi\sin\beta & \sin\psi & \cos\beta\cos\psi \end{bmatrix} \tag{16}$$

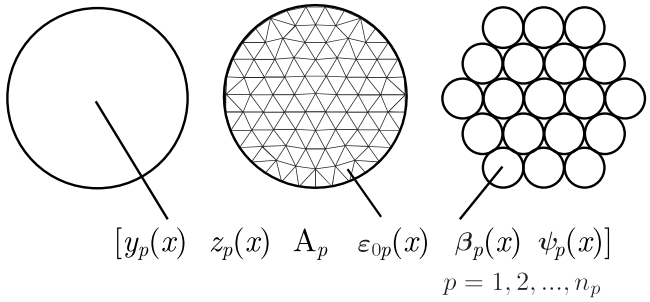

Fig. 4. Different levels of tendon fiber discretization.

Since the fiber strain vector $\boldsymbol{\varepsilon}_m$ refers to the cross-section axes x, y, z, it is necessary to project it onto the tendon. To make this consistent with the fiber section formulation, the rotation matrix defined in Eq. (15) is directly applied to the compatibility matrix $\mathbf{a}_s(y, z)$, computed as:

$$\bar{\mathbf{a}}_s(y, z) = \mathbf{R}\mathbf{a}_s(y, z) \tag{17}$$

Eq. (10) is thus generalized using Eq. (17) to evaluate material strains at the tendon level:

$$\boldsymbol{\varepsilon} = \bar{\mathbf{a}}_s\mathbf{e} + \boldsymbol{\varepsilon}_0 \tag{18}$$

After $\boldsymbol{\varepsilon}_0$ is introduced, the tendon behaves like any other fiber, and requires an appropriate constitutive law to evaluate the fiber stress vector and stiffness matrix:

$$\boldsymbol{\sigma}(x, y, z) = f[\boldsymbol{\varepsilon}(x, y, z)] \tag{19}$$

The contribution of tendons to the section stresses $\mathbf{s}$ are then evaluated as the integral of the fiber stresses $\boldsymbol{\sigma}$, and the section stiffness $\mathbf{k}$ as the integral of the fiber tangent stiffness $\mathbf{C}^t$. These result again from the application of the virtual work principle, as in [2]:

$$\mathbf{s} = \int_A \bar{\mathbf{a}}_s^T\, \boldsymbol{\sigma}\, \mathrm{d}A \approx \sum_{fiber} A_f \bar{\mathbf{a}}_s^T\, \boldsymbol{\sigma} \tag{20}$$

$$\mathbf{k} = \int_A \bar{\mathbf{a}}_s^T\, \mathbf{C}^t\, \bar{\mathbf{a}}_s\, \mathrm{d}A \approx \sum_{fiber} A_f \bar{\mathbf{a}}_s^T\, \mathbf{C}^t\, \bar{\mathbf{a}}_s \tag{21}$$

where A_f is the fiber area. The introduction of the tendons at the section level requires the definition of the following input data for each prestressing steel fiber: coordinates $y_p(x)$ and $z_p(x)$, fiber area A_p, initial strains $\varepsilon_{0p}(x)$ and angles $\beta_p(x), \psi_p(x)$ of the cable at x. This additional data are collected in a vector for every tendon fiber p for a total of n_p number of fibers per section:

$$\begin{matrix}[y_p(x) & z_p(x) & \mathrm{A}_p & \varepsilon_{0p}(x) & \beta_p(x) & \psi_p(x)] \\ & & & & p = 1, 2, \ldots, n_p & \end{matrix} \tag{22}$$

The model easily accounts for the presence of several cables with the required accuracy: one can indeed use one fiber for each tendon, or discretize the area of a single tendon into several fibers, or instead use one fiber for multiple tendons (Fig. 4). In most cases, it is sufficient to use a single fiber per tendon.

Given the shape of the tendons (for example parabolic shape for post-tensioned cables or piecewise linear for pre-tensioned tendons), $y_p(x)$ and $z_p(x)$ are a function of x as they may change at different integration points (IP). The controlled section position is given by the integration scheme (Gauss–Lobatto in this work). We recall that the model can suffer from loss of accuracy when few integration points are used. This issue is investigated in one of the validation studies (Section 6.1). Also, along the integration point length $w_i L$ the tendon position is constant (Fig. 5). This implies that for complex tendon layouts a high number of IP may be needed for a more accurate description of the tendon geometry.

3.1. Time-dependent phenomena

Short-term losses are considered instantaneous and can be applied before or during the analysis by properly reducing the initial fiber strain ε_0. This approach is in line with common design practices and can be used to account for anchorage set, friction between jacks, tendon, and concrete. PC elements and more specifically bridges are exposed to significant strain–stress state modifications over long time spans. Concrete shrinkage and creep, and cable relaxation have to be considered in any analysis. These effects are assessed in the design phase of prestressed structures, and their implementation in the proposed beam element uses consolidated code-provided functions. All time-dependent phenomena are added to the fiber initial strain vector $\boldsymbol{\varepsilon}_0$. These time-dependent strains are called $\boldsymbol{\varepsilon}_d(t)$ to distinguish them from the initial prestressing strains $\boldsymbol{\varepsilon}_0$ (assumed constant over time). The time-dependent strains are applied to the tendon fibers to model cable relaxation and concrete fibers to model creep and shrinkage. When time dependence is considered in the analysis, Eq. (10) is rewritten as:

$$\boldsymbol{\varepsilon}(t) = \bar{\mathbf{a}}_s\mathbf{e} + \boldsymbol{\varepsilon}_0 + \boldsymbol{\varepsilon}_d(t) \tag{23}$$

where the dependence on the coordinates x, y, z is omitted. The time-dependent strains $\boldsymbol{\varepsilon}_d(t)$ allow to represent different phenomena such as:

- cable relaxation: negative strains are applied to tendon fibers. This effect reduces the pretension in the cables;
- concrete shrinkage: positive strains are applied to concrete fibers. This effect produces tension in concrete and compression in steel, causing the entire element to shrink when equilibrium is enforced;
- concrete creep: positive strains are applied to concrete fibers to reduce compression proportionally to the applied stress, which is negative. This effect acts only on compressed fibers and further enhances the curvature in the beam.

An example is shown in Fig. 6 where positive strains are applied to a single tendon fiber. When creep and shrinkage are applied to concrete fibers, the other fibers corresponding to reinforcement and tendons are subjected to negative strains until equilibrium is attained in the whole element. The concrete fibers may be subjected to compression to balance the positive $\varepsilon_d(t)$ applied, as shown in Fig. 7.

4. 3D damage-plastic constitutive law for concrete

The 3D plastic-damage model proposed by Di Re et al. in [26] is used for the concrete fibers. This is a previous version of the concrete law presented in [25], where the plasticity is instead based on Von-Mises approach, and is an extension of the proposal in [24]. The main characteristics are recalled here. Given the six-component strain vector $\boldsymbol{\varepsilon}$, the work-conjugate stress vector $\boldsymbol{\sigma}$ is obtained through the following equation:

$$\boldsymbol{\sigma} = (1 - D)^2\mathbf{C}(\boldsymbol{\varepsilon} - \boldsymbol{\varepsilon}^p) = (1 - D)^2\mathbf{C}\boldsymbol{\varepsilon}^e = (1 - D)^2\bar{\boldsymbol{\sigma}} \tag{24}$$

where $\boldsymbol{\sigma}$ is the stress vector, $\boldsymbol{\varepsilon}$, $\boldsymbol{\varepsilon}^e$ and $\boldsymbol{\varepsilon}^p$ are the total, elastic and plastic strains, respectively; D is a scalar damage variable that ranges from 0 (that represents the undamaged elastic material state) to 1 (corresponding to a completely damaged material); $\mathbf{C}$ is the 6×6 elastic constitutive matrix and $\bar{\boldsymbol{\sigma}}$ is the effective stress vector.

The tangent constitutive matrix $\mathbf{C}^t$, according to [28], may be obtained through the differentiation of the stress vector with respect to the strain vector, resulting in:

$$\dot{\boldsymbol{\sigma}} = \left[(1 - D)^2\mathbf{C}^{ep} - 2(1 - D)\mathbf{C}\boldsymbol{\varepsilon}^e \frac{\partial D}{\partial \boldsymbol{\varepsilon}}\right] \dot{\boldsymbol{\varepsilon}} = \mathbf{C}^t\dot{\boldsymbol{\varepsilon}} \tag{25}$$

where $\mathbf{C}^{ep}$ is the tangent elasto-plastic 6×6 stiffness matrix.

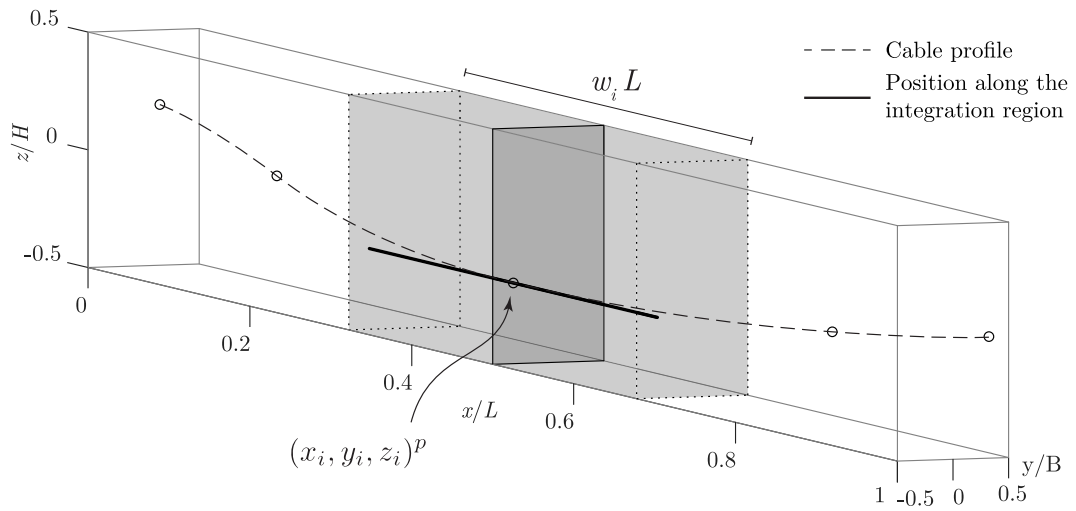

Fig. 5. Example of tendon profile with 5 Gauss–Lobatto integration points. The position of the pth tendon fiber y_i, z_i for each integration point x_i is constant throughout the whole region $w_i L$.

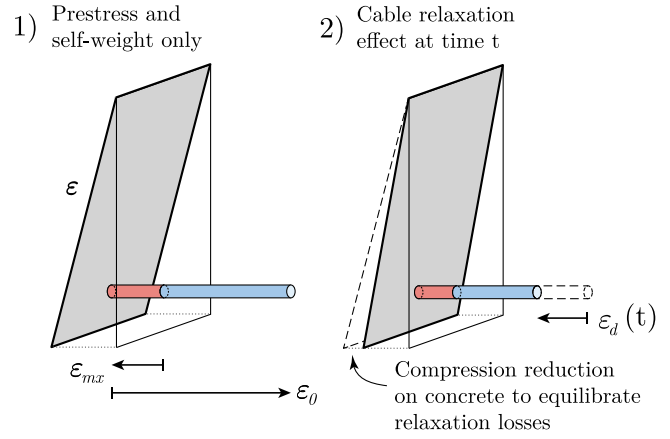

Fig. 6. Section strain distribution when the negative time-dependent strain ϵ_d is applied to a tendon fiber. Since the tendon tension reduces, compression in the concrete fibers reduces too as a result of equilibrium.

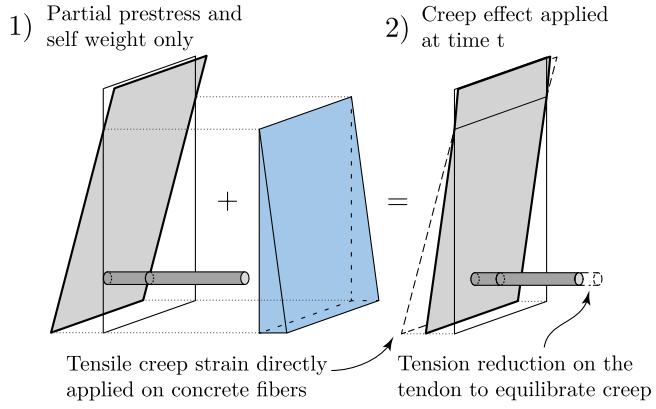

Fig. 7. Positive $\epsilon_d(t)$ for creep applied to concrete fibers. If the section top is in tension (top), $\epsilon_d(t)$ causes a bilinear $\epsilon_x(y, z)$ profile and additional negative strains at all the other fibers to balance the creep effects.

4.1. Plastic model

As for the plastic evolution problem, given the strain vector, the plasticity flow is ruled by the following Drucker–Prager yield function:

$$f(\boldsymbol{\eta}, \alpha) = |\boldsymbol{\eta}| - \sqrt{\frac{2}{3}}(\sigma_y + H_i \alpha) + \mu J_1 \tag{26}$$

where $\boldsymbol{\eta} = \mathbf{P}\bar{\boldsymbol{\sigma}} - \boldsymbol{\zeta}$, $\mathbf{P}$ is an operator that extracts the deviatoric part of the effective stress vector $\bar{\boldsymbol{\sigma}}$ and $\boldsymbol{\zeta}$ is the back-stress vector; σ_y is the yield threshold, H_i is the isotropic hardening parameter, α is the back-stress variable, μ the friction coefficient and $J_1 = \mathbf{1}^T \bar{\boldsymbol{\sigma}}$ is the stress first invariant, with $\mathbf{1}$ denoting the 6-component column vector used to extract the volumetric part of the effective stress.

The evolution of the plastic variables is governed by the following equations:

$$\dot{\boldsymbol{\epsilon}}^p = \dot{\lambda}\frac{\partial f}{\partial \boldsymbol{\sigma}}, \quad \dot{\alpha} = \sqrt{\frac{2}{3}}\dot{\lambda}, \quad \dot{\boldsymbol{\zeta}} = \frac{2}{3} H_k \dot{\boldsymbol{\epsilon}}^p \tag{27}$$

where λ is the plastic multiplier, evolving according to the Karush–Kuhn–Tucker complementarity and consistency conditions:

$$\dot{\lambda} \geq 0, \quad f \leq 0, \quad \dot{\lambda} f = 0, \quad \dot{\lambda}\dot{f} = 0 \tag{28}$$

and H_k is the kinematic hardening parameter.

Table 1
Elastic and plastic parameters for concrete used in Fig. 8.

Elastic and plastic parameters					
E [GPa]	ν	H_k	H_i	σ_t [MPa]	σ_c [MPa]
30	0.2	$0.5E$	0.1E	3.3	15

Table 2
Damage parameters for concrete used in Fig. 8.

Damage parameters						
Y_{t0}	a_t	b_t	Y_{c0}	a_c	b_c	β
7.92×10^{-5}	0.8	8×10^{-5}	3.6×10^{-4}	0.1	5×10^{-3}	1

The tangent elastoplastic matrix is computed as:

$$\mathbf{C}^{ep} = \mathbf{C} - \frac{4G^2\dot{\lambda}}{\eta}\left(\mathbf{I} - \frac{1}{3}\mathbf{1}\mathbf{1}^T - \hat{\mathbf{n}}\hat{\mathbf{n}}^T\right) - \frac{4G^2\hat{\mathbf{n}}\hat{\mathbf{n}}^T + 6GK\mu\hat{\mathbf{n}}\mathbf{1}^T}{2G + \frac{2}{3}\left(H_i + H_k\right)} \tag{29}$$

where $\mathbf{I}$ is the 6×6 identity matrix. The material parameters G and K are the shear and bulk moduli, respectively.

4.2. Damage model

To account for the unilateral effects due to the re-closure in compression of the tensile cracks, two different damage variables are

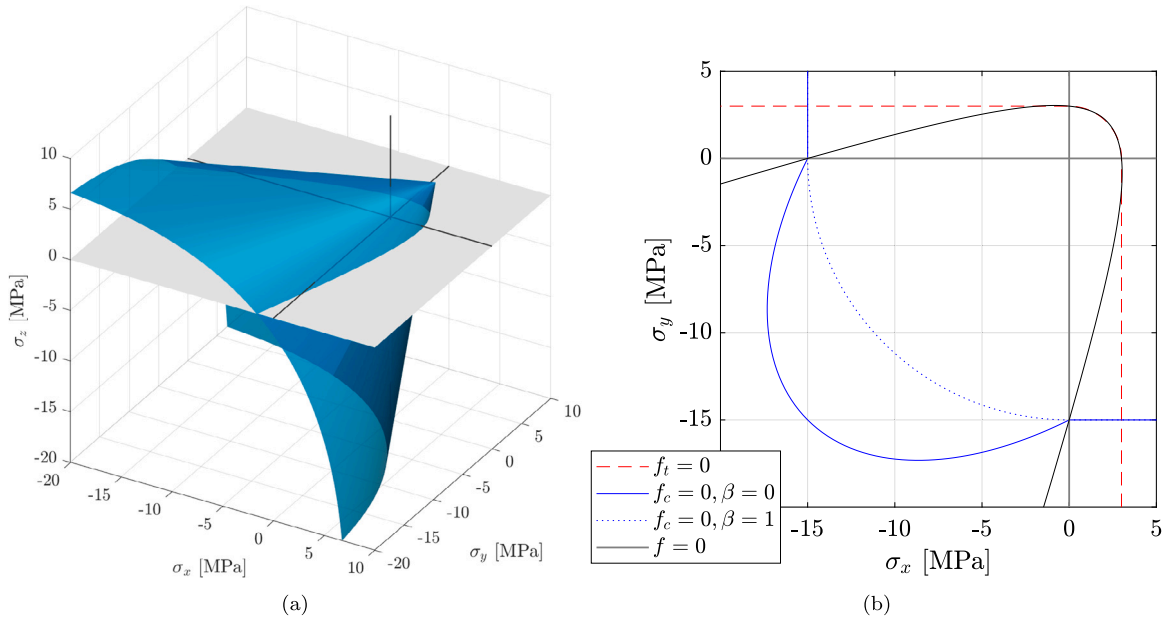

Fig. 8. Plastic and damage domains using the parameters in Tables 1 and 2: (a) 3D Drucker–Prager yield surface; (b) Damage limit function and plastic envelope for the plane-stress condition $\sigma_z = 0$.

used, D_t and D_c, that measure damage for prevailing tensile and compressive states, respectively. These evolve independently satisfying the constraint $D_t \geq D_c$. Both range between 0 and 1 and satisfy the thermodynamic irreversibility conditions $\dot{D}_t \geq 0$ and $\dot{D}_c \geq 0$. The damage-associated variables, Y_t, Y_c, Y_t^e and Y_c^e are defined as:

$$Y_t = \sqrt{\sum_{i=1}^{3} \langle e_i \rangle_+^2}, \quad Y_t^e = \sqrt{\sum_{i=1}^{3} \langle e_i^e \rangle_+^2}, \tag{30}$$

$$Y_c = \sqrt{\sum_{i=1}^{3} \langle e_i \rangle_-^2 - \beta \sum_{j \neq i=1}^{3} \langle e_i \rangle_- \langle e_j \rangle_-} \tag{31}$$

$$Y_c^e = \sqrt{\sum_{i=1}^{3} \langle e_i^e \rangle_-^2 - \beta \sum_{j \neq i=1}^{3} \langle e_i^e \rangle_- \langle e_j^e \rangle_-} \tag{32}$$

where brackets $\langle \bullet \rangle_\pm$ compute the positive/negative part of the quantity, and β is a material parameter influencing the shape of the damage limit function in compression. The terms e_i and e_i^e are evaluated from the principal total strains, $\hat{\varepsilon}_i$, as well as the elastic strains, $\hat{\varepsilon}_i^e$, respectively, as:

$$e_i = (1 - 2\nu)\hat{\varepsilon}_i + \nu \sum_{j=1}^{3} \hat{\varepsilon}_j \tag{33}$$

$$e_i^e = (1 - 2\nu)\hat{\varepsilon}_i^e + \nu \sum_{j=1}^{3} \hat{\varepsilon}_j^e \tag{34}$$

The overall damage variable D is the linear combination of D_t and D_c:

$$D = \alpha_t D_t + \alpha_c D_c \tag{35}$$

where the two weight factors α_t and α_c are evaluated as:

$$\alpha_t = \frac{\eta_t^2}{\eta_t^2 + \eta_c^2}, \quad \alpha_c = \frac{\eta_c^2}{\eta_t^2 + \eta_c^2} = 1 - \alpha_t \tag{36}$$

and

$$\eta_h = \frac{Y_h^e}{Y_{0h} + D(a_h Y_h^e + b_h)} \tag{37}$$

where $h = t, c$ for tension and compression, respectively. The damage limit functions in tension and compression are defined as:

$$f_h(Y_h, D_h) = Y_h - Y_{0h} - D_h(a_h Y_h + b_h) \tag{38}$$

Table 3
Elastic and plastic parameters for concrete and steel.

Fiber	Elastic and plastic parameters					
	E [GPa]	ν	H_k	H_i	σ_t [MPa]	σ_c [MPa]
Concrete	30	0.2	$0.7E$	0	3	60
Steel	210	0.3	0	0	450	450
Tendon	195	0.3	0	0	1325	1325

where the evolution of D_h, follows the Karush–Kuhn–Tucker conditions:

$$\dot{D}_h \geq 0, \quad f_h \leq 0, \quad \dot{D} f_h = 0, \quad \dot{D}_h \dot{f}_h = 0 \tag{39}$$

The constitutive law requires 13 parameters:

- 2 for the elastic behavior: the Young's modulus E and the Poisson's ratio ν;
- 4 for the plastic model: the compression and tension yielding thresholds σ_c and σ_t, the kinematic hardening parameter H_k and the isotropic hardening parameter H_i that control the yielding and back-stress rates, respectively;
- 7 for the damage model: Y_{0h} controlling the strain value where damage starts, b_h, that controls the maximum material strengths, a_h, that mainly controls the softening branches, and β, that is a parameter that influences the shape of the damage limit function in compression.

The limit domains corresponding to the parameters in Tables 3 and 4 are shown in Figs. 8(a) and 8(b), while a uni-axial cyclic test is shown in Fig. 9(a) for the axial behavior and Fig. 9(b) for the shear behavior. Due to the isotropic nature of the adopted damage model, the overall damage variable D equally affects all the components of the 3D constitutive matrix. Then, also the shear behavior is regulated by the D variable, where the effects of D_t and D_c are properly weighted.

5. Computational aspects

5.1. Force-based element implementation

The element state determination follows the iterative FB algorithm proposed in [2] and implemented in OpenSees [31]. The nonlinear

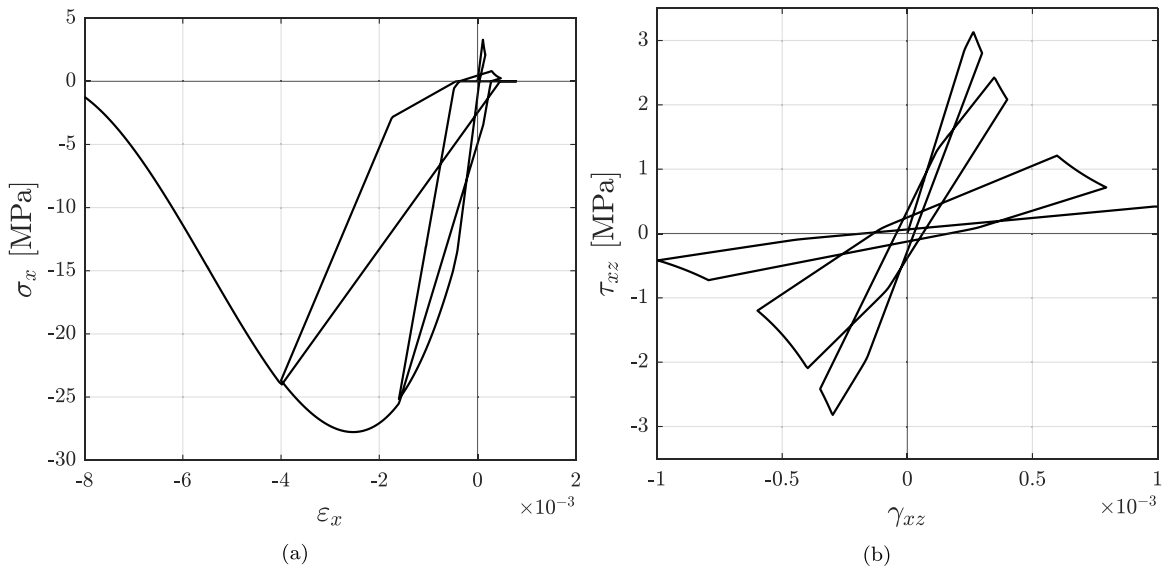

Fig. 9. Uni-axial damage-plastic cyclic test for concrete with the parameters in Tables 1 and 2: (a) Axial test on ε_x; (b) Shear test on γ_{xz}.

solution procedure at the global iteration i is briefly recalled here. The element iterations j start with $\Delta\mathbf{v}^{j=1} = \Delta\mathbf{v}^{i}$. The element nodal forces $\Delta\mathbf{q}^{j}$ are computed using the last computed flexibility matrix $\mathbf{F}^{j-1}$. Using Eq. (8), it follows:

$$\Delta\mathbf{q}^{j} = \mathbf{F}^{j-1}\Delta\mathbf{v}^{j} \tag{40}$$

The element forces are updated as:

$$\mathbf{q}^{j} = \mathbf{q}^{j-1} + \Delta\mathbf{q}^{j} \tag{41}$$

For each section (integration point), the increment of the section stresses are updated by means of Eq. (3):

$$\Delta\mathbf{s}^{j} = \mathbf{b}\,\Delta\mathbf{q}^{j} \tag{42}$$

$$\mathbf{s}^{j} = \mathbf{s}^{j-1} + \Delta\mathbf{s}^{j} \tag{43}$$

The section strain increment $\Delta\mathbf{e}^{j}$ is computed from the last computed section flexibility matrix $\mathbf{f}^{j-1}$ and the strain residuals $\mathbf{r}^{j-1}$ evaluated at the previous element iteration:

$$\Delta\mathbf{e}^{j} = \mathbf{r}^{j-1} + \mathbf{f}^{j-1}\Delta\mathbf{s}^{j} \tag{44}$$

$$\mathbf{e}^{j} = \mathbf{e}^{j-1} + \Delta\mathbf{e}^{j} \tag{45}$$

where $\mathbf{r}^{0} = \mathbf{0}$.

For each fiber, the state determination starts from computing the fiber strains $\boldsymbol{\varepsilon}^{j}$ from Eq. (23):

$$\boldsymbol{\varepsilon}^{j} = \bar{\boldsymbol{a}}_{s}\, \boldsymbol{e}^{j} + \boldsymbol{\varepsilon}_{0} + \boldsymbol{\varepsilon}_{d}^{i} \tag{46}$$

We recall that the initial strains $\boldsymbol{\varepsilon}_0$ are constant throughout the analysis, while $\boldsymbol{\varepsilon}_d^i$ is taken as constant during the global iteration. The resulting fiber strains are stored in 6-component vectors. The stress vectors for all fibers are evaluated using the 3D damage-plastic law presented in Section 4 for the concrete fibers, and the classical J2 plasticity law for the reinforcement and the tendon fibers. To link the 3D stress–strain formulation at the fiber level with the generalized beam model at the section level, a static condensation is required to pass from the six strain, $\boldsymbol{\varepsilon}$, and stress, $\boldsymbol{\sigma}$, components to $\boldsymbol{\varepsilon}_k = [\varepsilon_x, \gamma_{xy}, \gamma_{xz}]^T$ and $\boldsymbol{\sigma}_k = [\sigma_x, \tau_{xy}, \tau_{xz}]^T$ respectively. The iterative process described in [35] is followed. This process involves the total stress and strain vectors and the incremental stress–strain relation in Eq. (25), partitioned according to the vector components to be retained, indicated with subscript k, and the vector components to be condensed out, indicated with subscript c, as follows:

$$\begin{bmatrix}\Delta\boldsymbol{\sigma}_k\\ \Delta\boldsymbol{\sigma}_c\end{bmatrix} = \begin{bmatrix}\mathbf{C}_{kk} & \mathbf{C}_{kc}\\ \mathbf{C}_{ck} & \mathbf{C}_{cc}\end{bmatrix}\begin{bmatrix}\Delta\boldsymbol{\varepsilon}_k\\ \Delta\boldsymbol{\varepsilon}_c\end{bmatrix} \tag{47}$$

The condensed strain vector $\boldsymbol{\varepsilon}_c = [\varepsilon_y, \varepsilon_z, \gamma_{yz}]^T$ is found by imposing $\boldsymbol{\sigma}_c = [\sigma_y, \sigma_z, \tau_{yz}]^T = \mathbf{0}$. In other words, confinement is neglected. The material tangent stiffness matrix is:

$$\mathbf{C}_k^t = \mathbf{C}_{kk} - \mathbf{C}_{kc}\left(\mathbf{C}_{cc}\right)^{-1}\mathbf{C}_{ck} \tag{48}$$

and the incremental stress–strain relation is:

$$\Delta\boldsymbol{\sigma}_k = \mathbf{C}_k^t\Delta\boldsymbol{\varepsilon}_k \tag{49}$$

An elasto-plastic predictor phase is required to compute the evolution of the plastic variables according to the Karush–Kuhn–Tucker conditions, by considering the damage evolution as frozen. It results:

$$\begin{cases}\Delta\boldsymbol{\varepsilon}_p = \Delta\lambda\hat{\mathbf{n}}\\ \Delta\alpha = \sqrt{\frac{2}{3}}\Delta\lambda \quad \text{if } f > 0\\ \boldsymbol{\zeta} = \frac{2}{3}H_k\boldsymbol{\varepsilon}^p\end{cases} \tag{50}$$

Once the plastic strain and hardening variables increments have been computed, the damage progression is evaluated. A damage corrector phase follows to evaluate the updated damage variables in tension and compression, D_t and D_c, and eventually, the damage:

$$D_t = \frac{Y_t - Y_{t0}}{a_t Y_t + b_t} \quad D_c = \frac{Y_c - Y_{c0}}{a_c Y_c + b_c} \tag{51}$$

An iteration loop is required at the fiber level (from Eq. (47) to Eq. (51) indicated with l in Algorithm 1). Convergence is reached when $\boldsymbol{\sigma}_c$ become sufficiently small.

The resisting section forces $\mathbf{s}_r^j$ and the section tangent stiffness $\mathbf{k}^j$ are computed as the sums of the fiber contributions over the section:

$$\mathbf{s}_r^j \approx \sum \bar{\boldsymbol{\alpha}}_{\mathbf{s}}^T\boldsymbol{\sigma}_k\mathrm{A}_f \tag{52}$$

$$\mathbf{k}^j \approx \sum \bar{\boldsymbol{\alpha}}_{\mathbf{s}}^T\mathbf{C}_k\bar{\boldsymbol{\alpha}}_s\mathrm{A}_f \tag{53}$$

The section unbalanced forces $\mathbf{s}_u^j$ are then evaluated as:

$$\mathbf{s}_u^j = \mathbf{s}^j - \mathbf{s}_r^j \tag{54}$$

In conclusion, the section residual strains are evaluated using the section flexibility matrix $\mathbf{f}^j$ as:

$$\mathbf{r}^j = \mathbf{f}^j\,\mathbf{s}_u^j = \left(\mathbf{k}^j\right)^{-1}\,\mathbf{s}_u^j \tag{55}$$

The element flexibility is computed using Eq. (9) and the element stiffness $\mathbf{K}^j = \left(\mathbf{F}^j\right)^{-1}$. The displacement increments for the next element iteration (if needed) are then computed from the section residual strains. If the element convergence is not reached, the steps (Eq. (40) to Eq. (55)) are repeated. The modified section and fiber state determination steps are summarized in Algorithm 1.

Algorithm 1: Section and fiber state determination algorithms.

Data: Section integration properties, history variables
for every integration point **do**
  Section stress vector increment interpolated from element forces $\Delta\mathbf{s}^j = \mathbf{b}\Delta\mathbf{q}^j$
  Section strain vector increment using flexibility from last iteration $\Delta\mathbf{e}^j = \mathbf{r}^{j-1} + \mathbf{f}^{j-1}\Delta\mathbf{s}^j$
  Total section strains $\mathbf{e}^j = \mathbf{e}^{j-1} + \Delta\mathbf{e}^j$
  for every fiber **do**
    Fiber strains from fiber compatibility $\boldsymbol{\epsilon}^j(x,y,z) = \mathbf{a}_s\mathbf{e}^j + \boldsymbol{\epsilon}_0 + \boldsymbol{\epsilon}_d^i$
    while $l < l_{max}$ & $|\boldsymbol{\sigma}_c| > tol$ **do**
      Full strain vector $\boldsymbol{\epsilon}^l$
      Elasto-plastic predictor phase
      $\begin{cases} \Delta\boldsymbol{\epsilon}_p = \Delta\lambda\hat{\mathbf{n}} \\ \Delta\alpha = \sqrt{\frac{2}{3}}\Delta\lambda \quad \text{if } f > 0 \\ \zeta = \frac{2}{3}H_k\boldsymbol{\epsilon}^p \end{cases}$
      Damage corrector phase $D_t = \frac{Y_t - Y_{t0}}{a_t Y_t + b_t}$ $D_c = \frac{Y_c - Y_{c0}}{a_c Y_c + b_c}$
      Concrete/steel constitutive law
    end
    Fiber stress vector $\boldsymbol{\sigma}^j = \{\sigma_x\tau_{xy}\tau_{xz}\}$
    Fiber stiffness through static condensation $\mathbf{C}_k^{t\,j} = \mathbf{C}_{kk} - \mathbf{C}_{kc}\mathbf{C}_{cc}^{-1}\mathbf{C}_{ck}$
  end
  Section resisting stress vector $\mathbf{s}_r^j = \sum \bar{\mathbf{a}}_s^T\boldsymbol{\sigma}^j\mathrm{A}_f$
  Section stiffness $\mathbf{k}^j = \sum \bar{\mathbf{a}}_s^T\mathbf{C}_k^{t\,j}\bar{\mathbf{a}}_s\mathrm{A}_f$
  Unbalanced section stresses $\mathbf{s}_u^j = \mathbf{s}^j - \mathbf{s}_r^j$
  Section residual strains $\mathbf{r}^j = (\mathbf{k}^j)^{-1}\mathbf{s}_u^j$
end

5.2. Regularization technique

The Gauss integration rule is commonly used in FE formulations. However, in frame elements undergoing special loading conditions where usually the section stresses attain their maximum values at the element ends, the Gauss–Lobatto rule is preferred in order to directly control the element end sections. In addition, since cementitious composite structures generally exhibit a softening behavior, localization of strains and damage can emerge [24]. In case of force-based approaches the size of the localization regions is typically determined by the adopted integration rule [3]. This can lead to non objective numerical results and strongly dependent on the selected rule. To overcome this numerical pathology and obtain objective results, the modified integration rule proposed in [3,30], is here introduced. According to [3], the element is divided into three regions, where the two end regions can have 2 or 3 Gauss–Lobatto integration points and lengths L_c/w_1, with L_c and w_1 denoting the characteristic length and the weight associated to the first Gauss-Lobatto point. The order of accuracy is $2n-3$, for each region, being n the number of points per region.

Following [30], a Gauss–Lobatto distribution is used for the whole element but two more points are added within the expected localization region. Their weights are $w_1(L - L_c)$, so that L_c can be unlimited, and the Lobatto distribution is restored in the rest of the beam. The order of accuracy however reduces to $n-3$.

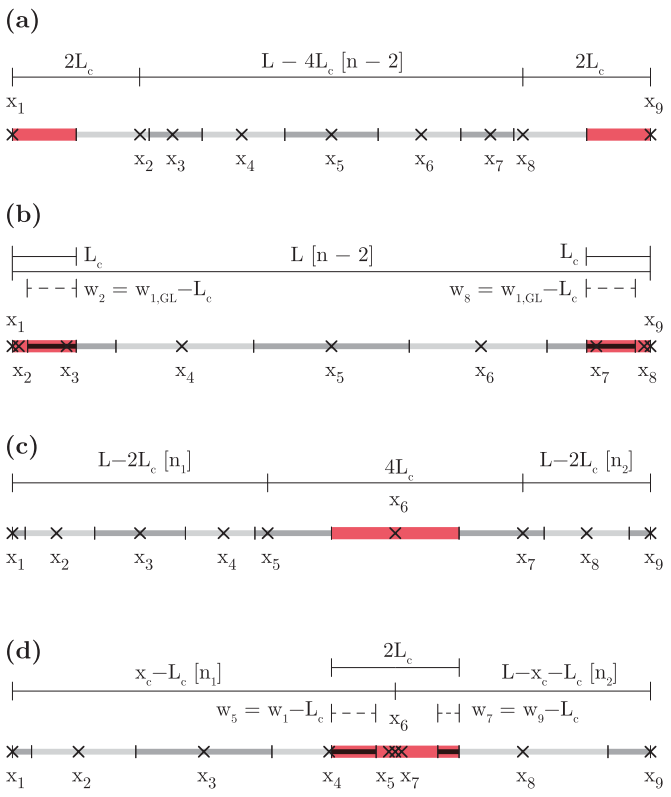

Fig. 10. 9-point Gauss–Lobatto regularized integration schemes proposed by: (a) Addessi and Ciampi [3]; (b) Scott and Hamutçuoğlu [30]. Proposed extended distributions for: (c) scheme [3]; (d) scheme [30].

The key parameter is the characteristic length L_c, that governs the size of the localization region. This is usually taken as the plastic hinge length, and can be evaluated by adopting existing formulae, as described in Bazant et al. [36], but also in Almeida et al. [37] and Feng et al. [38]. In common design practice, L_c is assumed to be approximately $d/2$ for older buildings and d for new constructions with additional shear reinforcement at the elements' ends, with d being the section's effective depth. In this paper L_c is taken as $0.8H$, with H being the section's depth, since it deals with beams designed according to current codes. The two regularization techniques described above are schematically shown in Fig. 10(a) and (b). The methods become particularly efficient when using single and slender elements in seismic frames, as stated by the authors, since the localization is typically expected to occur at the end sections. Here, an extension is proposed to allow localization to occur at any integration point along the beam. It still requires the analyst to choose beforehand the integration points where the damage can localize. If the localization point x_c is internal, it divides the beam in two regions and the other integration points are properly redistributed. Some examples of the integration scheme arrangements are shown in Fig. 10(c) and (d), respectively.

6. Case studies and applications

The model presented in the previous sections is used to carry out nonlinear static analyses to validate it and show its capabilities. First of all, a theoretical test is carried out in Section 6.1 to verify the regularization procedure presented in Section 5 on a simple PC cantilever beam. A PC beam with a draped cable is presented in Section 6.2. The influence of the number of integration points and the characteristic length for the regularization are tested for accuracy. Correlation studies

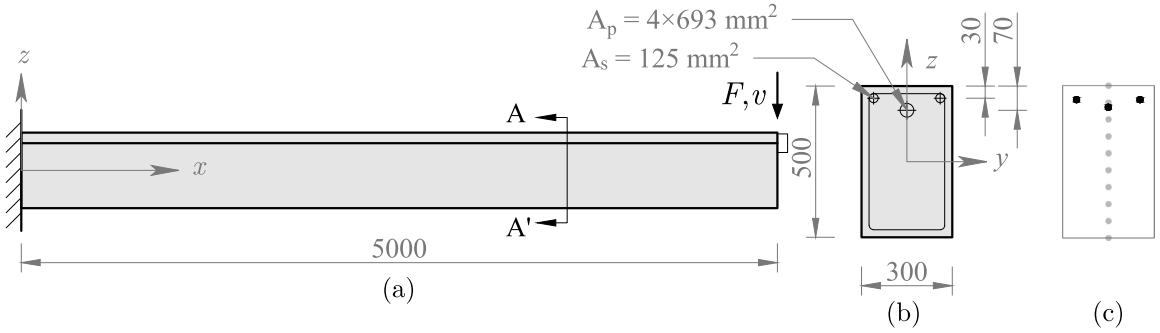

Fig. 11. Geometry of the PC cantilever beam: (a) longitudinal view; (b) cross-section A-A'; (c) fibers' location.

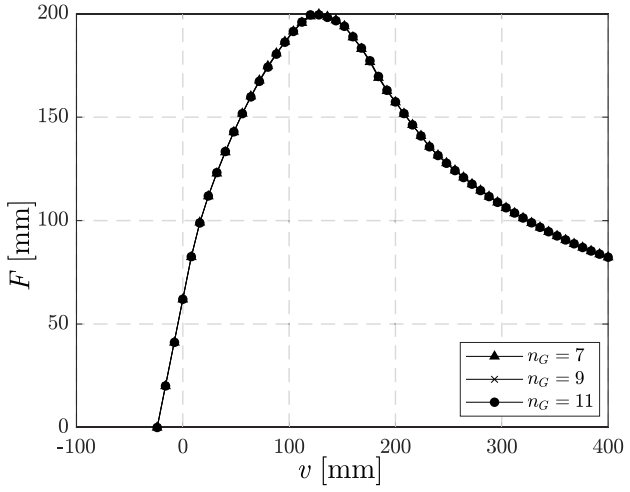

Fig. 12. Displacement-controlled tests on the cantilever beam in Fig. 11 with different numbers of integration points.

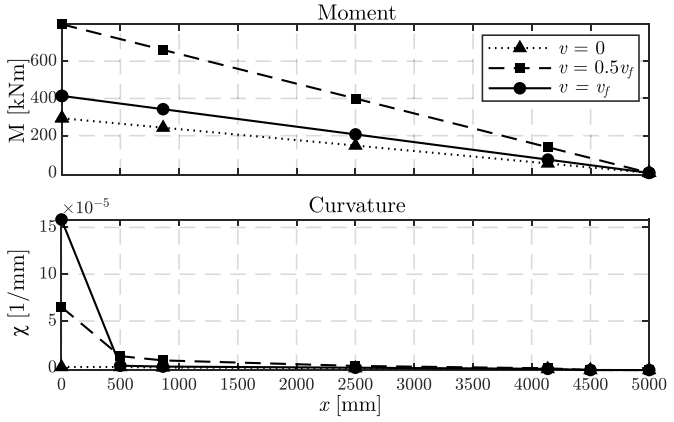

Fig. 13. Moment and curvature distributions at specific steps of the global response curves in Fig. 12 with 7 integration points.

with experimental results are presented next: the first one concerns a simply supported PC beam with a bonded draped cable, the second one focuses on the time-dependent phenomena (that is creep, shrinkage, and steel relaxation) that develop over a few years.

6.1. PC cantilever beam

A pushover test on a simple PC cantilever beam is carried out. This is a theoretical case for the validation of the proposed regularization technique. The prestressing cable area is large enough to apply a high compression force to the beam. Severe softening is expected due not only to progressive section cracking, but also to compression damage in the concrete. The beam geometry is shown in Fig. 11. The tendon is straight and its position in the cross-section is constant along the beam. Two different tests are carried out, the first one using the concrete 3D damage plastic model of Section 4 (3DDP) and the second one using the 1D model by Yassin [39] (1DD). The first test uses a Timoshenko beam formulation, the second one uses an Euler–Bernoulli formulation. Since the cantilever beam of Fig. 11 is slender, the shear strains should be negligible. The concrete compression and tension strengths are $f_{cc} = -38$ MPa and $f_{ct} = 3$ MPa, respectively. The concrete and steel properties are reported in Tables 3 and 4. The corresponding uni-axial tension and compression laws are shown in Fig. 14(b). There is no steel strain hardening. The prestressing is imposed by applying the initial strain $\varepsilon_0 = 0.005$, that corresponds to the stress $\sigma_0 = E_p\varepsilon_0 = 975$ MPa applied before the beam shortens.

The regularization is carried out by modifying the layout of the mesh as described in Section 5.2, with the localization zone at $x_c = 0$ mm (the fixed end), and a characteristic length $L_c = 0.1L$. Fig. 12 shows the structural response of the cantilever beam where the vertical reaction F is measured with respect to an imposed displacement v up to a value $v_f = 400$ mm. The number of integration points varies as indicated in the legend of Fig. 12. Since there are only negligible differences, the element can be considered regularized.

Table 4
Damage parameters for concrete.

Fiber	Damage parameters						
	Y_{t0}	a_t	b_t	Y_{c0}	a_c	b_c	β
Concrete	2.16	0.9	10^{-4}	7.20	0.9	3.25×10^{-3}	1

The moment and curvature distributions along the beam in Fig. 13 show how the strains are correctly localized within the prescribed characteristic region.

As expected, changes in the localization length L_c only modify the softening branch without affecting the pre-peak response. Fig. 14(a) shows the curves for different values of L_c for both the damage-plasticity material 3DDP and the 1DD models. The two cases show a similar trend in the first part, since the two concrete laws have the same compression strength. Some differences as for the post-peak behavior are expected since the softening behavior is linear in 1DD and nonlinear in 3DDP. No losses are considered in this case.

6.2. PC beam with a draped tendon

A more complex tendon layout is studied next to verify that the positions and number of integration points do not affect the solution accuracy. The PC beam in Fig. 15 is used for this study. The original beam was experimentally tested and the results are reported in [40].

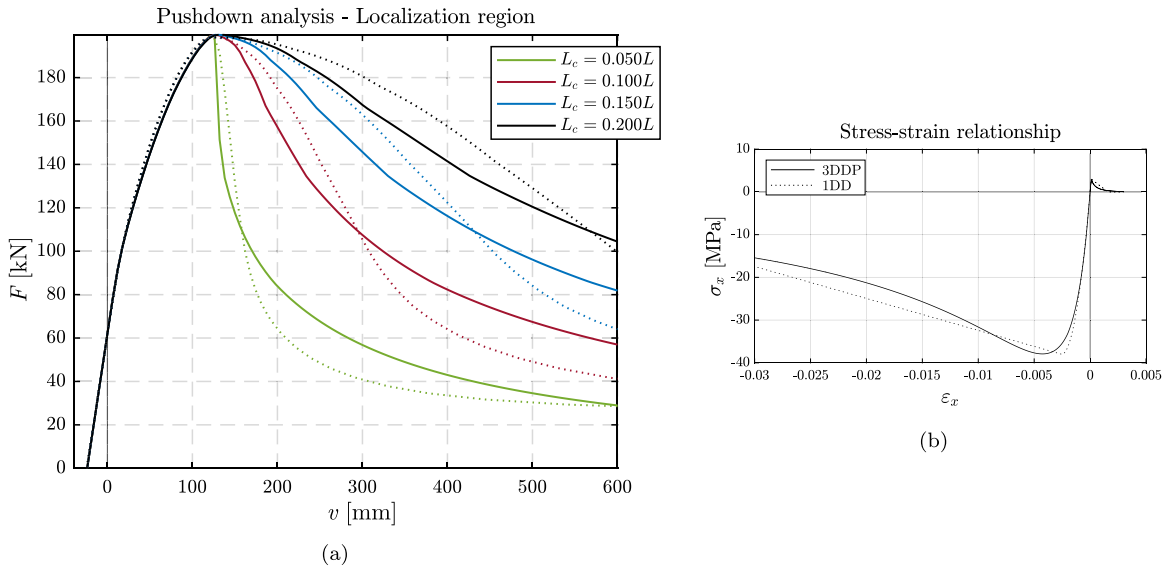

Fig. 14. (a) Pushover response curve of the PC cantilever beam in Fig. 11 with different L_c for the localization zone; (b) Concrete constitutive laws: plastic-damage model [26] and uni-axial concrete model with linear softening [39].

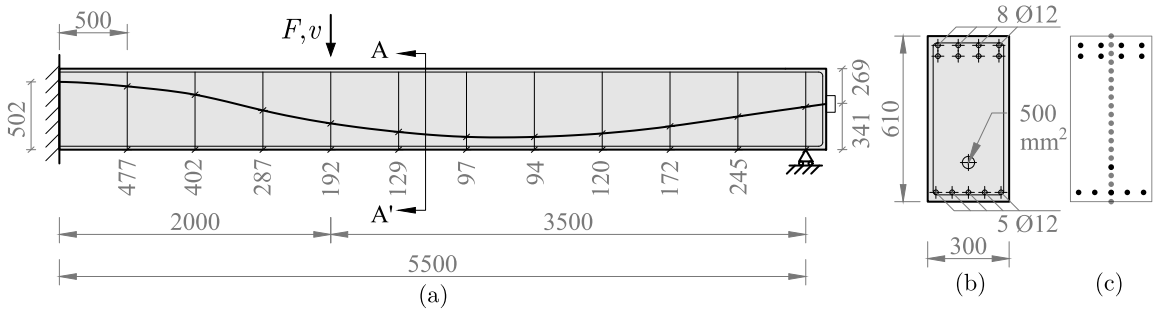

Fig. 15. Geometry of the PC beam with a draped tendon: (a) longitudinal view; (b) cross-section A-A'; (c) fibers numerical discretization.

Table 5
Elastic and plastic parameters for concrete and steel.

Fiber	Elastic and plastic parameters					
	E [GPa]	ν	H_k	H_i	σ_t [MPa]	σ_c [MPa]
Concrete	33	0.2	$0.7E$	$0.001E$	5	66
Steel	194.5	0.3	0	0	548	548
Tendon	190	0.3	0	0	1570	1570

Table 6
Damage parameters for concrete.

Fiber	Damage parameters						
	Y_{t0}	a_t	b_t	Y_{c0}	a_c	b_c	β
Concrete	3.6	0.99	10^{-3}	14.4	0.8	8×10^{-3}	1

Its geometry was adjusted to the scope of this study. There are 8 longitudinal top ⌀12 mm rebars and 5 bottom ⌀12 mm rebars. The tendon is made of three strands with a ⌀0.6" diameter, with a total area $A_p = 420$ mm^2. The cable position varies along the element. The load application node is at 2000 mm to the right of the fixed end. The applied prestressing corresponds to an initial strain $\varepsilon_0 = 0.0025$. The material properties for concrete and steel are reported in Tables 5 and 6, respectively.

The beam is initially loaded with its self-weight, applied as a uniformly distributed load, and with the prestressing force. A displacement-controlled test is carried out pushing the node at $x = 2000$ mm down to $z = -40$ mm. At this stage, the beam is cracked and is in its softening branch. Damage in concrete builds up mainly because of the increasing compression at the fixed end. A shear failure mode is observed numerically, in line with the experimental test, even though the geometry was slightly modified. Shear is very high in the first beam segment as the point of load application is close to the fixed support. The influence of the number of Gauss points and regularization technique is initially tested for a characteristic length equal to $L_c = 0.1L$. Two localization zones are considered in the first element, at $x = 0$ mm and $x = 2000$ mm, and one in the second element, at $x = 2000$ mm. The regularization length is then modified to show how it influences the slope of the softening branch. The stresses applied by the cable to the beam depend on the distribution of the Gauss points. In the global response reported in Fig. 16(a) the curves show slight changes as the number of Gauss points decreases. It is concluded that the solution already converges for 5 integration points. Convergence in terms of the total normalized potential energy of the system is also shown. Full convergence is reached with 7 integration points, even though 5 integration points produce a relatively small error.

The initial displacement due to self-weight and prestressing loads is negative (i.e. the beam bends upward). Fig. 16(b) shows the global response curves for different values of the characteristic lengths. The results confirm that, as the characteristic length L_c increases, the softening trend becomes less severe.

The experimental results proposed in [40] are compared to the numerical simulations. In this tests, the same double-T section of the experiment is used. A schematic representation of the beam is shown

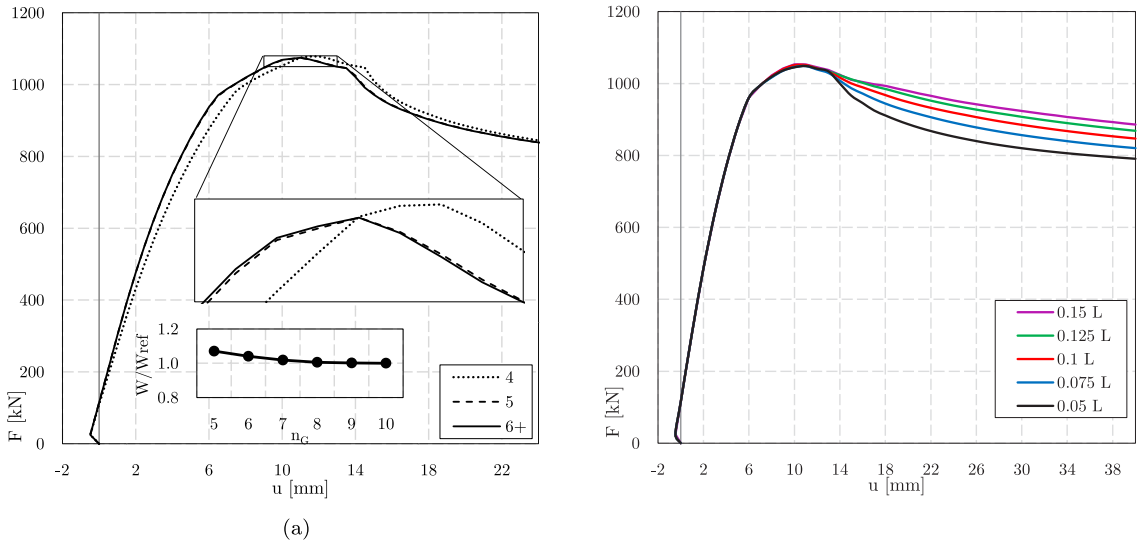

Fig. 16. (a) Force–displacement response curve for different numbers of integration points and $L_c = 0.04L$. The bottom plots shows the total energy, normalized with respect to the reference case ($n_G = 10$) - (b) Global response for increasing localization lengths L_c.

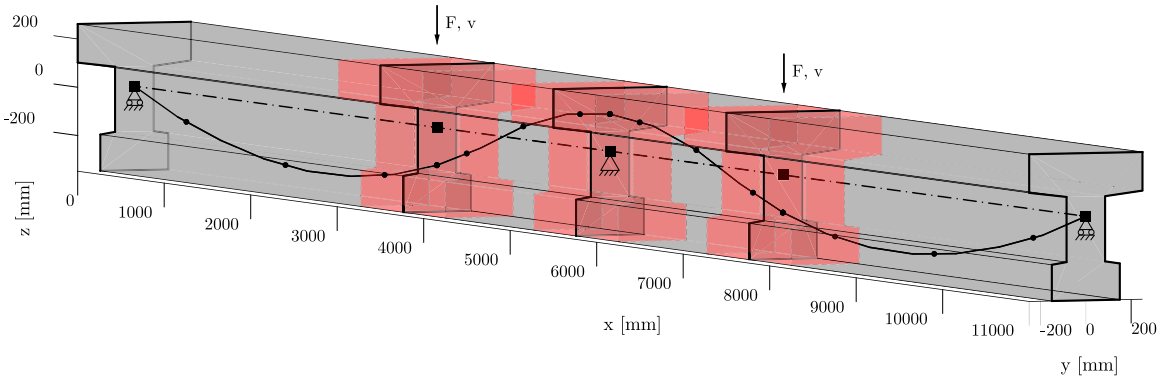

Fig. 17. Numerical model of the beam tested in Herbrand et al. [40].

in Fig. 17, adopting four FEs and 5 Gauss–Lobatto points for each of them, and $L_c = 0.0887L = 0.8H$. The material parameters are contained in Tables 5 and 6, with σ_t and σ_c set to match the concrete strengths reported in [40].

The response curves for three different cases, TB1, TB2, and TB3, under increasing axial load, are shown in Fig. 18. The original test was carried out using three beams that were 11 m long with a middle support. The loads were applied at $x = \pm 2000$ mm from the middle support, resulting in two tests obtained for each side of the beam. The element shear was monitored at $x = \pm 560$, mm, while the displacements were measured at the load application points.

Since the original beam collapses on one side and then on the other, lower stiffness in the experimental case is expected at the beginning. The numerical tests instead exhibit a higher amount since perfect symmetry is achieved. However, despite some slight differences, the numerical model behaves similarly to the experimental beam as for the formation of shear and flexural cracks. In the numerical structural response of Fig. 18, the stiffness reduction is partially due to the flexural damage in the support/loading zones, but mostly due to the shear damage in the web of the beam. Numerical collapse also occurs due to shear failure in the peak points, similarly to the experimental test. The damage occurring in the beam is shown in Fig. 19, which well matches the reported cracks pattern in [40]. The shear damage accumulates in the web according to the shear strain distribution, as explained in Section 3, here consistent with the double-T beam.

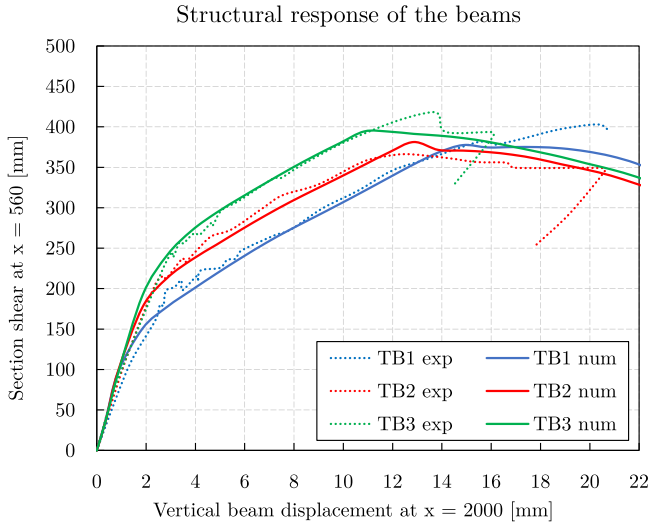

Fig. 18. Experimental (dot curves) and numerical (solid curves) global response curves for the three different beams TB1, TB2 and TB3 in [40] with increasing axial loads. The abscissa x is considered from the middle support.

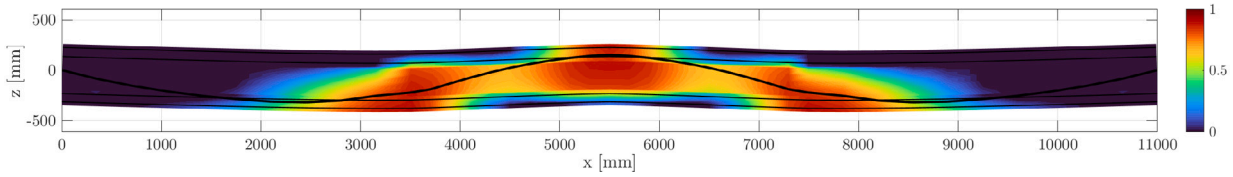

Fig. 19. Damage parameter D distribution over TB3 beam at $v = 5mm$.

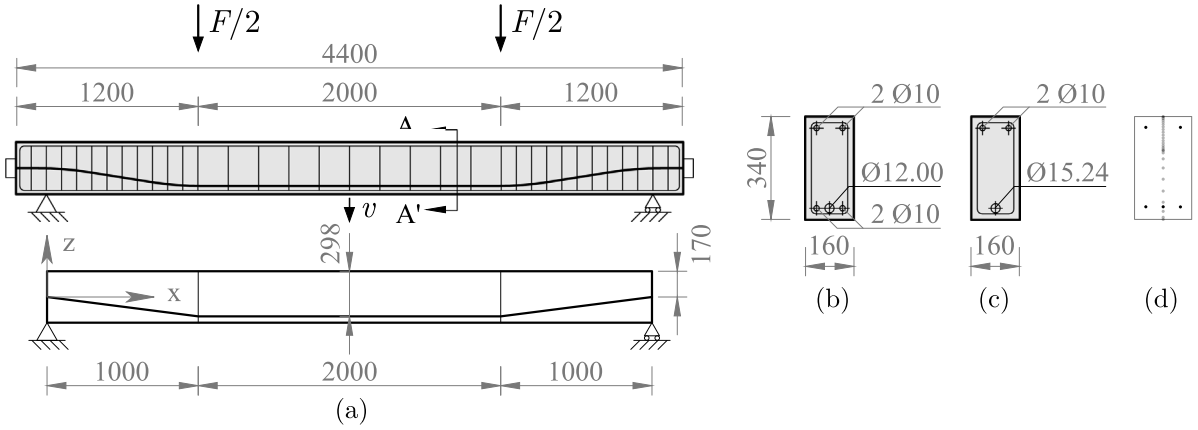

Fig. 20. Simply supported prestressed beam with a polygonal bonded tendon [33]: (a) longitudinal view; (b) cross-section A-A' of the beam B2-70-N-B; (c) cross-section A-A' of the beam B3-70-N-B; (d) fiber section discretization.

6.3. Four-point bending test on a PC beam

In this application the proposed element is used to reproduce the results of the experimental tests presented in [33]. The beam geometry is shown in Fig. 20. Two beams with a single fully bonded tendon are studied: they have different cross-sections, as shown in Fig. 20 (b) and (c). The bottom reinforcements and tendon areas are such that the total steel tensile force after yielding is the same in both beams. The prestressing index is provided in [33] and is computed as:

$$i_p = \frac{f_{py}A_p}{f_{py}A_p + f_{sy}A_s} \tag{56}$$

where f_{py} and f_{sy} are the yield stresses of tendon and reinforcement, respectively, while A_p and A_s are the corresponding areas.

In the numerical model, the beam is divided into 3 elements 1 m, 2 m, and 1 m long. The element self-weight is applied as a uniformly distributed load. The profile of the prestressing tendon is schematically shown in Fig. 20(a). The initial measured stress applied to the tendon is $\sigma_0 = 1127$ MPa at the ends and $\sigma_0 = 1000$ MPa at midspan, as reported in [33]. In the numerical model, the initial strain $\epsilon_0 = \sigma_0/E_p$ is imposed to the tendon, where E_p is the tendon elastic modulus.

The characteristic length assigned is assumed equal to $L_c = 0.068L = 0.8H$, as no other specific information is provided. Since it is small compared to the length of the central element, the integration scheme proposed in Addessi and Ciampi [3] is used with a localization point located at midspan ($x = 2000$ mm), as this position allows to use a higher number of integration points with the same maximum interpolation order. The tendon layout is simplified to a piece-wise linear pattern. 4, 9, 4 integration points are used in the three elements, with a regular distribution of integration points along the beam (Fig. 21).

The material parameters are those reported in Tables 7 and 8. A high-strength concrete with $f_{cc} = 75$ MPa is used for this beam. The uni-axial cyclic test is shown in Fig. 22.

In the experimental tests, all of the beams show bending failure. The same failure mode is observed in the numerical response reported in Fig. 23, where the vertical force F is shown as a function of the midspan vertical displacement v.

Table 7
Elastic and plastic parameters for concrete and steel.

Fiber	Elastic and plastic parameters					
	E [GPa]	ν	H_k	H_i	σ_t [MPa]	σ_c [MPa]
Concrete	33	0.2	$0.1E$	$0.01E$	2	100
Steel	200	0.3	$0.001E$	$0.001E$	470	470
Tendon	190	0.3	$0.003E$	$0.001E$	1674	1674

Table 8
Damage parameters for concrete.

Fiber	Damage parameters						
	Y_{t0}	a_t	b_t	Y_{c0}	a_c	b_c	β
Concrete	1.44	0.9	1.5×10^{-4}	14.4	0.2	1×10^{-2}	1

In Fig. 23, the displacements v are those due to F force only. In beam B2-70-N-B the failure mechanism is ductile and begins with yielding of the bottom reinforcement, followed by yielding of the prestressing tendon. The top compressed concrete progressively crashes. The changes in stiffness in the numerical responses of Figs. 23(a) and 23(b) clearly indicate the two yield points. They follow the same sequence documented in the experimental test. In beam B3-70-N-B (Fig. 23(b)), since there is no bottom reinforcement, only yielding of the tendon is observed, corresponding to the single sharp change of stiffness in the response. The first reduction in stiffness is due to the progressive decompression of the section, which leads to concrete cracking. The structural response of Beam B3-70-N-B exhibits peak strength similar to the previous beam, as it compensates for the lack of the bottom rebar with a larger prestressing cable, as stated in [33].

There are some discrepancies with the experimental response that can be observed in the yielding phases of the two beams, explained by the fact that the steel constitutive model (that is a Von Mises plasticity) has a sudden yield threshold while the prestressing steel typically shows a smoother trend at the beginning of the hardening phase. There are also slipping phenomena that are neglected in the numerical model. However, no considerable differences are observed. In the experiments, the beams show cracks between the two loading

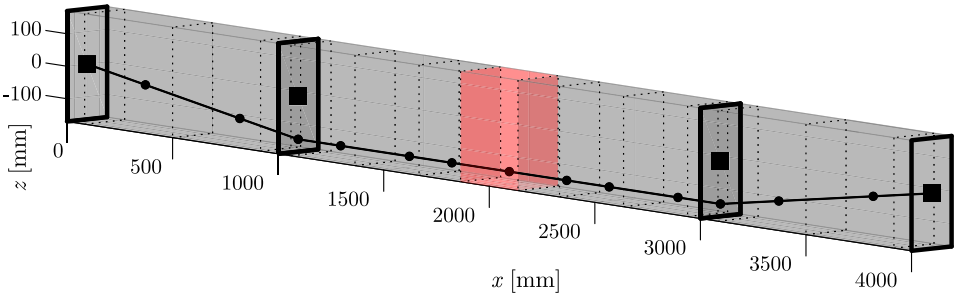

Fig. 21. Beam discretization; nodes, elements, integration points and localization region (colored). (For interpretation of the references to color in this figure legend, the reader is referred to the web version of this article.)

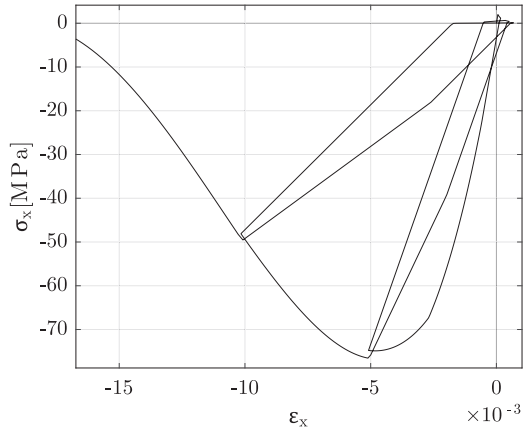

Fig. 22. Concrete constitutive law (f_{cc} = 75 MPa).

points, in the numerical cases the localization always takes place in the middle integration point, where the moment is maximum due to the beam self-weight. As the displacements gradually increase, the beam starts to lightly soften because the concrete contributes little to the overall response.

Representative section strain and stress distributions are shown in Fig. 24 at $v = 200$ mm. Fig. 24(a) shows the axial strains ε_x (computed according to Eq. (10)), Fig. 24(b) shows the axial stresses σ_x normalized with respect to $\sigma_y = f_{cc}$ for concrete and $\sigma_y = \sigma_t$ for steel in the mid-section at $x = 2000$ mm. Fig. 24(c) shows the parabolic distribution of the shear strains γ_{xz} and Fig. 24(d) shows the corresponding shear stresses τ_{xz} at $x = 1000$ mm. The highly nonlinear shear response is due the high damage occurring in the section.

At this level of deflection, the only non-zero stresses remain around the neutral axis while the rest of the section is completely damaged, as Fig. 25 shows.

6.4. Long term analysis and time-dependent effects on a PC beam

The proposed model includes the time-dependent effects that affect the structural behavior of PC beams, mainly shrinkage and creep in the concrete and relaxation in the cable. The above time-dependent phenomena are modeled as follows. Let us recall that the fiber strains are computed using Eq. (23) where ε_0 is the cable initial prestressing strain and $\varepsilon_d(t)$ accounts for the time-dependent effects. For concrete, the equations are those proposed in the Model Code for Concrete Structures [41] where the concrete time-dependent strain $\varepsilon_d(t)$ is expressed as:

$$\varepsilon_d(t) = \varepsilon_{cs}(t) + \varepsilon_{cc}(t) \tag{57}$$

with ε_{cs} being the shrinkage strain, and ε_{cc} the creep strain. The shrinkage strains depend exclusively on time and are easy to compute. On the other hand, the creep strains require special treatment since they depend on the stress applied to the tendon fiber, which in turn, depends on the strains.

The creep formulation follows the definition of a compliance function that contains the load application time t_0, the current time t, and other given environmental parameters. Times t_0 and t start from the time the concrete is cast. The creep function is expressed as:

$$\varepsilon_{cc}(t) = J(t,t_0)\sigma(t_0) + \int_{t_0}^{t} J(t,\tau)\frac{\partial\sigma(\tau)}{\partial\tau}d\tau \tag{58}$$

where the compliance function $J(t,\tau)$ is defined as:

$$J(t,\tau) = \frac{1}{E(t)} + \frac{\phi(t,\tau)}{E_{28}} \tag{59}$$

and $E(t)$ and E_{28} are the concrete Young's modulus at the generic time t and at $t = 28$ days, respectively, $\phi(t,\tau)$ is the creep coefficient and $\sigma(\tau)$ is the concrete stress at time τ. It results that, for each stress modification in the fibers, a variation of the creep strains is produced over time, determined by the evolution of the compliance function.

For its numerical implementation, Eq. (58) is written in incremental form, after derivation with respect to t and discretization. The following equation is obtained at time step t_{n+1}:

$$\varepsilon_{cc}^{n+1} = \varepsilon_{cc}^{n} + \Delta J\left(t^{n+1},t^0\right)\sigma_0 + \sum_{k=1}^{n}\Delta J\left(t^{n+1},t^k\right)\Delta\sigma^k \tag{60}$$

The last step of the analysis in the summation of Eq. (60) is omitted: this allows to determine the closed form expression for the creep strains at step t^{n+1}, considering the whole load history up to step t^n. For implementation, the equation can also be written in its total form:

$$\varepsilon_{cc}^{n+1} = \left[J\left(t^{n+1},t^0\right) - \frac{1}{E\left(t^{n+1}\right)}\right]\sigma_0 + \sum_{k=1}^{n} J\left(t^{n+1},t^k\right)\Delta\sigma^k \tag{61}$$

A similar approach is used for the cable relaxation strains $\varepsilon_{d,p}(t)$, even though the load variation in the prestressing cables is moderate and such that it can be neglected, thus only the losses for a constant tension $\sigma_p(t_0)$ can be considered:

$$\varepsilon_{d,p}(t) = J(t,t_0)\sigma_p(t_0) \tag{62}$$

To show the time-dependent behavior of the concrete and prestressing tendon, a simple concrete truss with section area $A_c = 100 \times 100$ mm^2 and a centered, straight tendon with diameter $D_p = 10$ mm is studied first and the results are shown in Fig. 26. The beam is cast at $t = 0$ days and an initial ε_0 is applied at $t = 7$ days. At $t = 40$ days, the prestressing action is increased up to $2\varepsilon_0$. At $t = 80$ days, the prestressing strain is completely removed and residual strains can be observed. Both differential (Eq. (60)) and total (Eq. (61)) creep formulations are used to compute the beam axial strain ε.

The last example is a PC beam experimentally monitored for time-dependent effects over a long time period. The beam geometry is

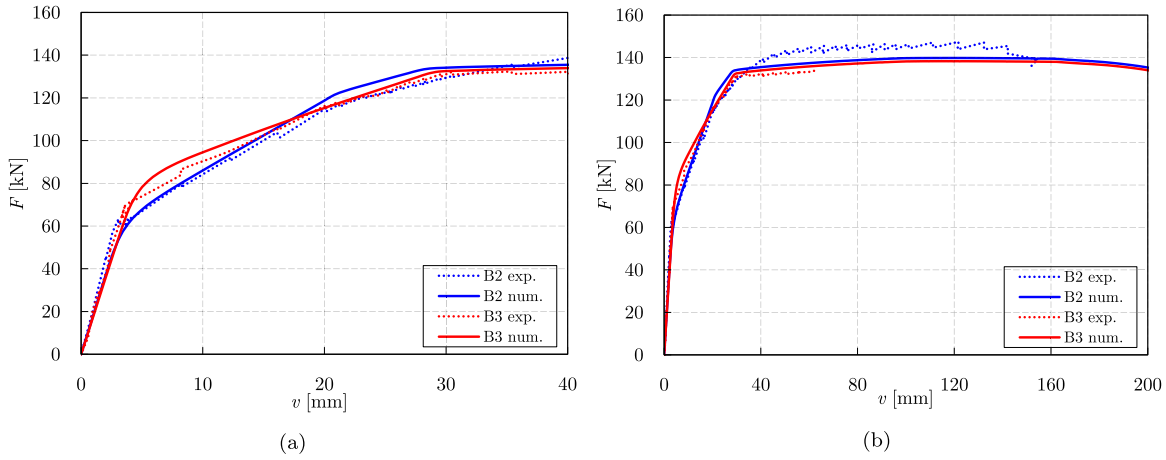

Fig. 23. Numerical (solid curves) and experimental (dot curves) pushover tests on beams B2-70-N-B and B3-70-N-B; Global response curves $F - v$ (midspan displacement) for: (a) displacements up to 40 mm; (b) displacements up to 200 mm.

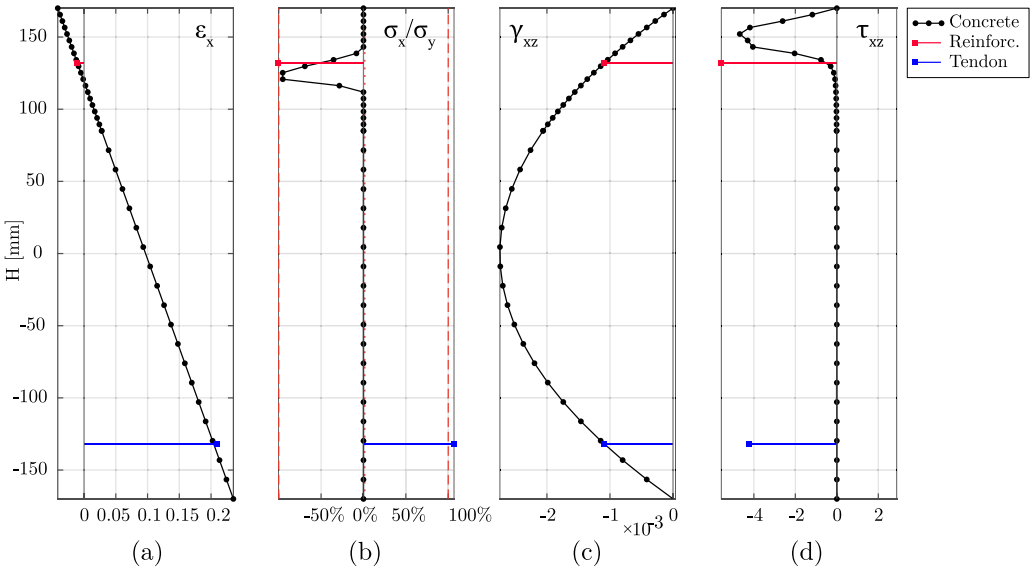

Fig. 24. Fiber strains and stresses at two sections of beam B3-70-N-B at $v = 200$ mm: (a) resulting axial strains ϵ_x and (b) normalized stresses σ_x/σ_y at $x = 2000$ mm, (c) shear strains γ_{xz} and (d) shear stresses τ_{xz} at $x = 1000$ mm.

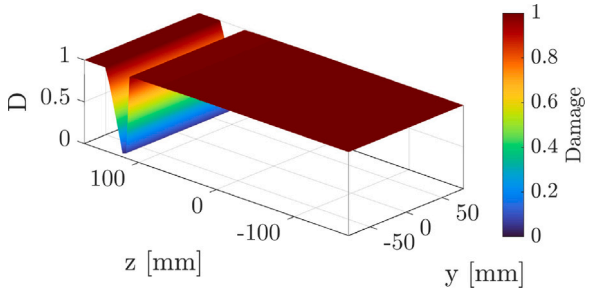

Fig. 25. Concrete damage in the mid-section for beam B3-70-N-B at $v = 200$ mm.

shown in Fig. 27 and the original experimental study is presented in Breckenridge and Bugg [34]. It is a double-T beam with two pre-stressing cables with a draped layout. The beam is modeled with only

Table 9
Elastic and plastic parameters for concrete and steel.

Fiber	Elastic and plastic parameters					
	E [GPa]	ν	H_k	H_i	σ_t [MPa]	σ_c [MPa]
Concrete	23.3	0.2	$0.7E$	$0.01E$	70	3
Steel	200	0.3	$0.005E$	$0.001E$	460	460
Tendon	169	0.3	$0.01E$	$0.001E$	1006	1006

1 element, 9 integration points and 36 fibers per section. This high number of integration points is selected for a detailed description of the tendon geometry. The beam discretization is shown in Fig. 28. The beam self-weight is initially applied as a uniformly distributed load. The original paper by Breckenridge and Bugg [34] provides the initial tendon stress σ_0 that corresponds to a uniformly applied strain $\epsilon_0 = \sigma_0/E_p = 689.5/169000.0 = 0.0041$. The material parameters are reported in Tables 9 and 10. A high-strength concrete with $f_{cc} = 43$ MPa is used. The uni-axial cyclic law is reported in Fig. 29.

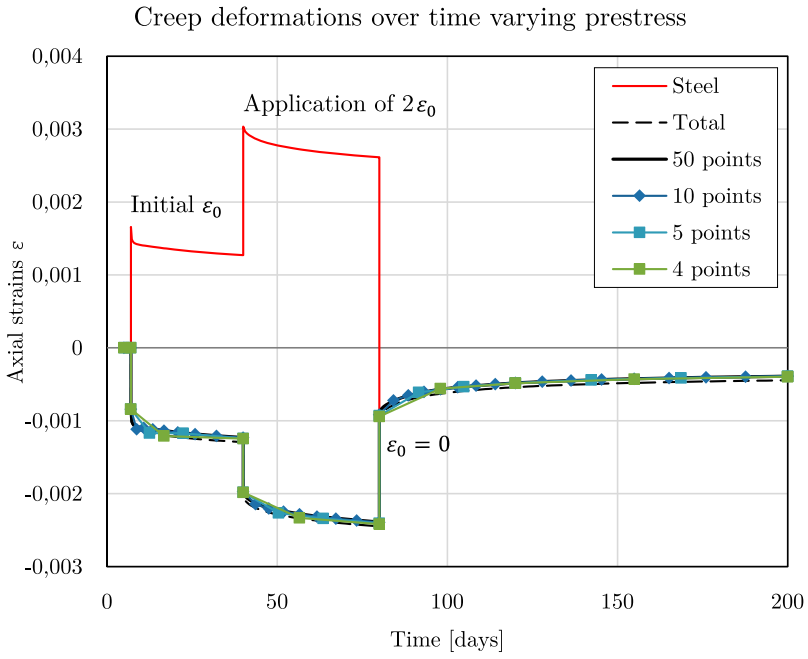

Fig. 26. Concrete axial strains on a simple PC truss only due to prestressing. The red curve represents the axial strain in the steel fiber, where the peaks occur following application of prestressing. Two prestressing strain increments are applied to the steel fiber: ε_0 at $t = 7$ days, and $2\varepsilon_0$ at $t = 40$ days. The other curves, denoted with total and the increasing number of time intervals used, represent the axial strain of the beam, which shrinks due to creep. (For interpretation of the references to color in this figure legend, the reader is referred to the web version of this article.)

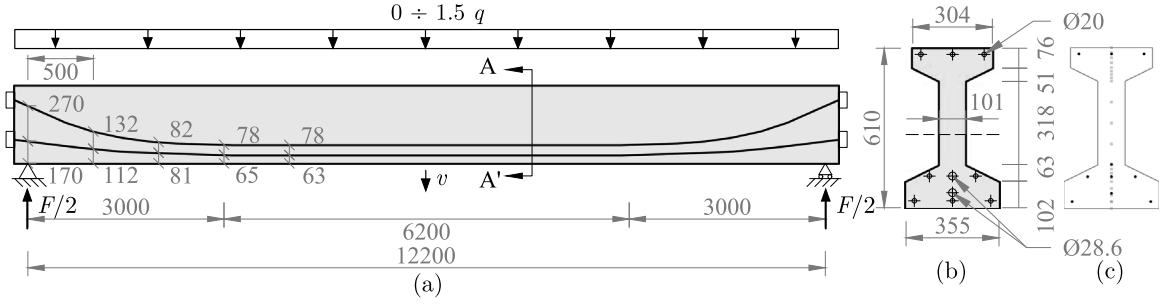

Fig. 27. Geometry of the PC beam with two fully bonded draped tendons [33]: (a) longitudinal view; (b) cross-section A-A' of the beam B2-70-N-B; (c) fibers' location.

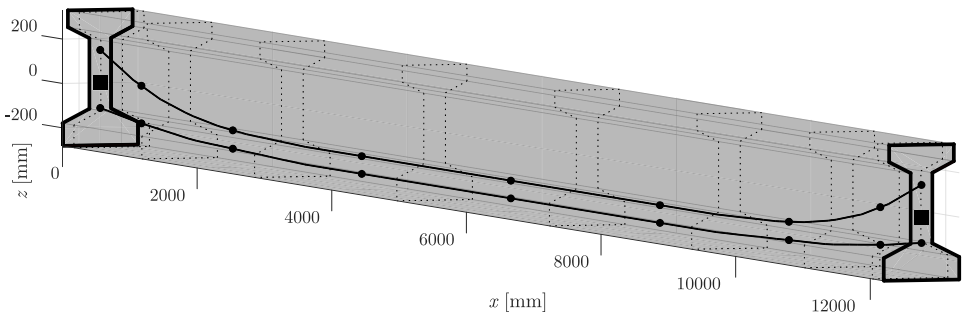

Fig. 28. Discretization of the PC beam: 1 element and 9 Gauss–Lobatto integration points.

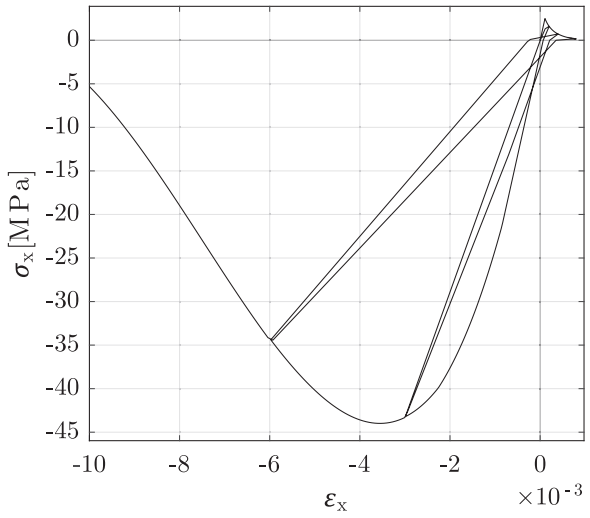

Fig. 29. Concrete constitutive law for $f_{cc} = 43$ MPa.

Table 10
Damage parameters for concrete.

Fiber	Damage parameters						
	Y_{t0}	a_t	b_t	Y_{c0}	a_c	b_c	β
Concrete	2.16	0.8	10^{-4}	14.4	0.1	7×10^{-3}	1

In the experimental campaign [34], 4 different values of the distributed load are analyzed: $0.0q$, $0.5q$, $1.0q$ and $1.5q$, where $q = 11.1$ N/mm. The beam is loaded in a 2-phase process and the global response curve in terms of the vertical reaction F versus vertical displacement v is shown in Fig. 30 for load $1.0q$. The results are obtained applying assuming average environmental conditions for the Model Code formulas. These are the same conditions reported in [33], that are: concrete age at prestressing $t_0 = 8$ days, relative humidity $UR = 70$, effective section height $h_0 = 107.9$ mm. In the first phase, the initial prestressing and the self-weight are applied instantly (point A). After 12 days pass [34] (point B), displacements v and curvature χ_y increase positively in the whole beam. The creep in the concrete increases them, while the concrete shrinkage and the cable relaxation decrease them. In the second step, the uniformly distributed load q is applied instantly (point C) and the resulting curvature is negative at mid-span and positive at the end sections, while the displacements are almost null. This induces the upper fibers to start creeping and the lower fibers to recover in the central sections. After point C, the beam is monitored for 7 years, similarly to the experimental test, producing negative displacements at mid-span and reaching a midspan deflection v of over 40 mm (point D).

The curves in Fig. 31 show both the experimental and numerical results. A good overlap is observed, although some differences emerge in some of the load cases reported. Observing the experimental results only, the trend of the displacement is not uniform over time since it depends on many factors, many more than those considered in classical time-dependent phenomena formulas, such as the seasonal temperature changes and the relative humidity fluctuations, briefly discussed in [34] and neglected in this paper. For these reasons, some approximations are to be expected and are deemed acceptable.

Fig. 32 shows the axial strains and stresses at midspan, at $t = 7$ years for load $1q$. Even though the section is completely compressed at the load application time, the creep effects carry the beam to a strain state where concrete begins to crack. The red lines refer to the reinforcement fibers, that are the only fibers without additional strains ε_0, therefore they are the only fibers where the strains equal mechanical strains. The blue lines refer to the tendons. Only the concrete in the compressed part of the section is affected by creep: this explain the nonlinear trend across the section.

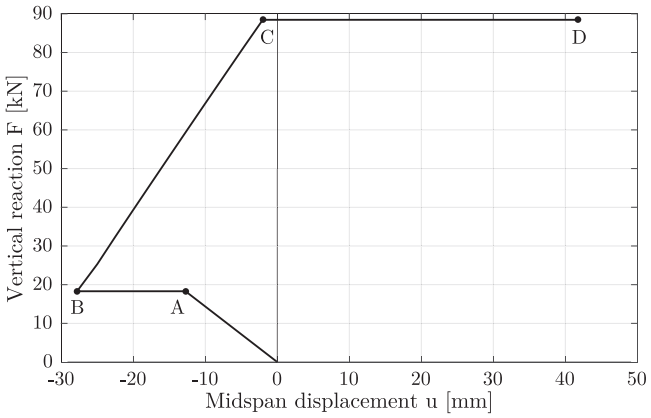

Fig. 30. Global response: (A) prestressing and self-weight are applied; (B) response after 12 days; (C) q is applied; (D) response after 7 years.

Fig. 33 shows the final distribution of concrete damage after 7 years at midspan. Although no additional information is provided in [34] about the final state of the beams, the numerical results indicate that the increase of the positive strains caused by the creep in the lower part of the section causes damage to emerge.

7. Summary and conclusions

A force-based fiber beam element for prestressed concrete structural members is presented in this paper. The model is a 3D Timoshenko beam which considers hysteretic hardening phenomena in steel as well as damage in concrete with a full 3D constitutive law, which allows to consider section shear strains alongside axial strains. The model is intended for fully bonded tendons.

Prestressing is easily applied through initial equivalent strains and the element contains an algorithm that allows any tendon profile to be inserted. The tendons are treated as additional fibers, and a rotation matrix allows to consider tendons that are not normal to the cross-section. The results confirm that the element works well with as low as five integration points. However, for complex cable geometry, additional integration points are needed for a better description of the tendon profile. The extension of an existing local regularization technique shows that regularization can be applied to any integration point, without affecting the numerical efficiency of the element.

Time dependent effects are considered at the fiber level and their effects are shown through examples including a comparison with four cases of an available experimental test campaign. An appropriate number of applications and case studies are presented and used to validate the model and discuss its characteristics.

The paper shows that the proposed element is accurate both in the case of nonlinear static an time dependent analyses. It has a low computational demand: all tests reported required short time to run. A limited number of elements, integration points and fibers can be used: in several cases, the number of integration points depends on the complexity of the geometry of the cable. The formulation is numerically stable, even when the response softens. The element can be used in the analysis of bridges and prestressed concrete structures in general.

Future possible enrichments of the model include: application to the study of prestressed concrete infrastructures including long term and nonlinear seismic analyses up to failure; extension to partially bonded tendons with bond–slip; extension to external tendons; extension to prestressed steel-concrete composite beams; application in the dynamic field as for example the seismic assessment of bridges.

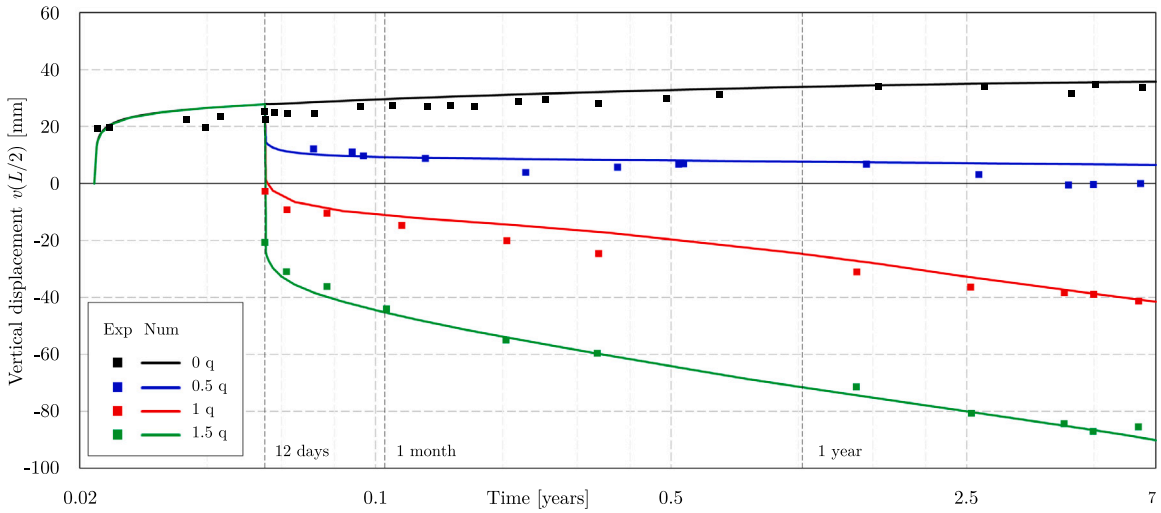

Fig. 31. Midspan vertical displacements over a 7 year span for different distributed loads.

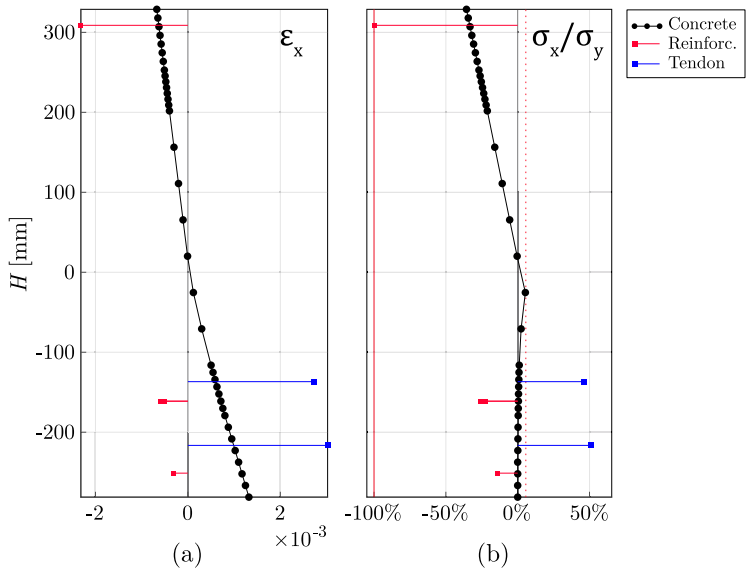

Fig. 32. Axial strains from Eq. (14) and normalized axial stresses at midspan for $1q$ load case at $t = 7$ years.

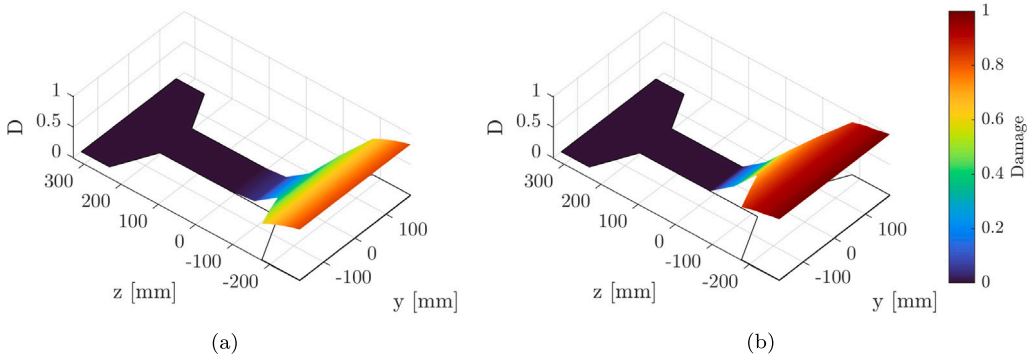

Fig. 33. Accumulated concrete damage at midspan for $1.0q$ load case at (a) $t = 1$ year, (b) $t = 7$ years.

CRediT authorship contribution statement

Luca Parente: Conceptualization, Methodology, Software, Validation, Original draft preparation. **Daniela Addessi:** Conceptualization, Methodology, Investigation, Supervision, Reviewing and editing. **Enrico Spacone:** Conceptualization, Methodology, Investigation, Supervision, Reviewing and editing, Project administration.

Declaration of competing interest

The authors declare that they have no known competing financial interests or personal relationships that could have appeared to influence the work reported in this paper.

Data availability

Data will be made available on request.

References

[1] Zeris CA, Mahin SA. Analysis of reinforced concrete beam & columns under uniaxial excitation. J Struct Eng 1988;114(4):804–20.
[2] Spacone E, Filippou FC, Taucer FF. Fibre beam–column element for non-linear analysis of R/C concrete frames: Part I: Formulation. Earthq Eng Struct Dyn 1996;25(7):711–25.
[3] Addessi D, Ciampi V. A regularized force-based beam element with a damage–plastic section constitutive law. Internat J Numer Methods Engrg 2007;70(5):610–29.
[4] Åldstedt E, Bergan PG. Nonlinear time-dependent concrete-frame analysis. J Struct Div 1978;104(7):1077–92.
[5] Limkatanyu S, Spacone E. Reinforced concrete frame element with bond interfaces. I: Displacement-based, force-based, and mixed formulations. J Struct Eng 2002;128(3):346–55.
[6] Taylor RL, Filippou FC, Saritas A, Auricchio F. A mixed finite element method for beam and frame problems. Comput Mech 2003;31(1):192–203.
[7] Feng DC, Wu G, Ning C-L. A regularized force-based Timoshenko fiber element including flexure-shear interaction for cyclic analysis of RC structures. Int J Mech Sci 2019;160:59–74.
[8] Feng DC, Ren X. Implicit gradient-enhanced force-based timoshenko fiber element formulation for reinforced concrete structures. Internat J Numer Methods Engrg 2021;122(2):325–47.
[9] Feng DC, Chen X, McKenna F, Taciroglu E. Consistent nonlocal integral and gradient formulations for force-based timoshenko elements with material and geometric nonlinearities. J Struct Eng 2023;149(4):04023018.
[10] Aalami BO. Load balancing: A comprehensive solution to post-tensioning. ACI Struct J 1990;87(6).
[11] Picard A, Massicotte B, Bastien J. Relative efficiency of external prestressing. J Struct Eng 1995;121(12):1832–41.
[12] Ayoub A, Filippou FC. Mixed formulation of bond-slip problems under cyclic loads. J Struct Eng 1999;125(6):661–71.
[13] Ayoub A, Filippou FC. Mixed formulation of nonlinear steel-concrete composite beam element. J Struct Eng 2000;126(3):371–81.
[14] Ayoub A. Nonlinear analysis of reinforced concrete beam-columns with bond-slip. J Eng Mech 2006;132(11):1177–86.
[15] Ayoub A, Filippou FC. Finite-element model for pretensioned prestressed concrete girders. J Struct Eng 2010;136(4):401–9.
[16] Vu N, Castel A, François R. Response of post-tensioned concrete beams with unbonded tendons including serviceability and ultimate state. Eng Struct 2010;32(2):556–69.
[17] Kim KS, Lee DH. Nonlinear analysis method for continuous post-tensioned concrete members with unbonded tendons. Eng Struct 2012;40:487–500.
[18] Moreira LS, Sousa JBM, Parente E. Nonlinear finite element simulation of unbonded prestressed concrete beams. Eng Struct 2018;170:167–77.
[19] Doty HA. A module for finite element analysis of prestressed concrete bridges. Boulder, USA: Department of Civil, Environmental and Architectural Engineering, University of Colorado; 2001.
[20] Kwak HG, Seo YJ. Numerical analysis of time-dependent behavior of pre-cast pre-stressed concrete girder bridges. Constr Build Mater 2002;16:49–63.
[21] Au FT, Si X. Accurate time-dependent analysis of concrete bridges considering concrete creep, concrete shrinkage and cable relaxation. Eng Struct 2011;33(1):118–26.
[22] Lou T, Lopes SMR, Lopes AV. Nonlinear and time-dependent analysis of continuous unbonded prestressed concrete beams. Elsevier; 2013.
[23] Lou T, Lopes SM, Lopes AV. A finite element model to simulate long-term behavior of prestressed concrete girders. Finite Elem Anal Des 2014;81:48–56.
[24] Addessi D, Marfia S, Sacco E. A plastic nonlocal damage model. Comput Methods Appl Mech Engrg 2002;191(13):1291–310.
[25] Gatta C, Addessi D, Vestroni F. Static and dynamic nonlinear response of masonry walls. Int J Solids Struct 2018;155:291–303.
[26] Di Re P, Addessi D, Filippou FC. Mixed 3D beam element with damage plasticity for the analysis of RC members under warping torsion. J Struct Eng 2018;144(6):1–13.
[27] Drucker DC, Prager W. Soil mechanics and plastic analysis or limit design. Quart Appl Math 1952;10:157–65.
[28] Simo J, Ju J. Strain- and stress-based continuum damage models—I. Formulation. Int J Solids Struct 1987;23(7):821–40.
[29] Scott MH, Fenves GL. Plastic hinge integration methods for force-based beam & column elements. J Struct Eng 2006;132(2):244–52.
[30] Scott MH, Hamutçuoğlu OM. Numerically consistent regularization of force-based frame elements. Internat J Numer Methods Engrg 2008;76(10):1612–31.
[31] McKenna F, Fenves GL, Scott MH. Open system for earthquake engineering simulation. Berkeley: University of California; 2000.
[32] Petracca M, Candeloro F, Camata G. Scientific toolkit for opensees. Pescara, Italy: ASDEA Software Technology; 2017.
[33] Hussien O, Elafandy T, Abdelrahman A, Baky SA, Nasr E. Behavior of bonded and unbonded prestressed normal and high strength concrete beams. HBRC J 2012;8(3):239–51.
[34] Breckenridge R, Bugg S. Effects of long-time loads on prestressed concrete beams. PCI J 1964.
[35] Zienkiewicz O, Taylor R. The finite element method for solid and structural mechanics. The finite element method, Elsevier Science; 2013.
[36] Bažant ZP, Pijaudier-Cabot G. Measurement of characteristic length of nonlocal continuum. J Eng Mech 1989;115(4):755–67.
[37] Almeida J, Das S, Pinho R. Adaptive force-based frame element for regularized softening response. Comput Struct 2012;102–103:1–13.
[38] Feng DC, Ren X, Li J. Implicit gradient delocalization method for force-based frame element. J Struct Eng 2016;142(2):04015122.
[39] Yassin MHM. Nonlinear analysis of prestressed concrete structures under monotonic and cycling loads [Ph.D. thesis], Berkeley: University of California; 1994.
[40] Herbrand M, Classen M. Shear tests on continuous prestressed concrete beams with external prestressing. Struct Concr 2015;16(3):428–37.
[41] Taerwe L, Matthys S, et al. Fib model code for concrete structures. Ernst & Sohn, Wiley; 2013.